Anisotropic Hydrogel Degradation Enhances 3D Collective Mesenchymal Stromal Cell Alignment, Mechanotransduction and Osteogenic Differentiation

Claudia A. Garrido[1,2], Daniela S. Garske[1], Christian H. Bucher[1], Shahrouz Amini[2], Georg N. Duda[1], Katharina Schmidt-Bleek[1], Amaia Cipitria[2,3,4 (*)]

[1] Julius Wolff Institute for Biomechanics and Musculoskeletal Regeneration, Berlin Institute for Health at Charité – Universitätsmedizin Berlin, Berlin, Germany

[2] Max Planck Institute for Colloids and Interfaces, Potsdam, Germany

[3] Group of Bioengineering in Regeneration and Cancer, Biogipuzkoa Health Research Institute, San Sebastián, Spain

[4] IKERBASQUE, Basque Foundation for Science, Bilbao, Spain

(*) Correspondence: Amaia Cipitria, amaia.cipitriasagardia@bio-gipuzkoa.eus; amaia.cipitria@mpikg.mpg.de

Keywords: 3D patterned degradation, anisotropic dual crosslinking, alginate, primary human mesenchymal stromal cells (hMSC), collective cell alignment, osteogenic differentiation, mechanotransduction, YAP expression, YAP nuclear translocation

Abstract

Tissue engineering involves assembling cells and mimicking the complex anisotropic architecture of biological tissues to perform specific functions. This study explores the impact of patterned hydrogels with anisotropic degradation compared to single-phase materials on the potential of enhancing cell spreading, collective alignment, mechanotransduction and osteogenic differentiation

of encapsulated human mesenchymal stromal cells (hMSCs). Spatial patterns of degradable (Deg) and non-degradable (noDeg) subregions are formed by photolithography: UV-triggered thiol-ene crosslinking with matrix metalloprotease (MMP) sensitive peptides form Deg phases, while non-UV exposed regions result in Diels-Alder spontaneous click crosslinking and noDeg phases. 3D patterns in hydrogel degradation enhance hMSC spreading and allow collective cell alignment in Deg areas, while cells remain rounded with no alignment in noDeg regions. In addition, we observe a boosted osteogenic differentiation when compared to single-phase materials, as mid osteogenic markers (osteocalcin) are expressed at day 14 in anisotropic gels, whereas in single-phase only early osteogenic markers are found (osterix). Mechanosensing pathways were evaluated using the expression and localization of YAP. Deg sections in patterned materials have an enhanced nuclear translocation and higher YAP expression compared to single-phase Deg materials and noDeg sections. This effect is lost and no patterns in YAP expression and localization emerge when using an MMP-scramble peptide or no-RGD materials. These findings demonstrate that 3D patterns in alginate hydrogel degradation guide hMSC spreading, collective alignment, enhance YAP nuclear translocation and osteogenic differentiation. Mimicking tissue anisotropy in 3D patterned hydrogels could have broad applications in biofabrication and tissue engineering.

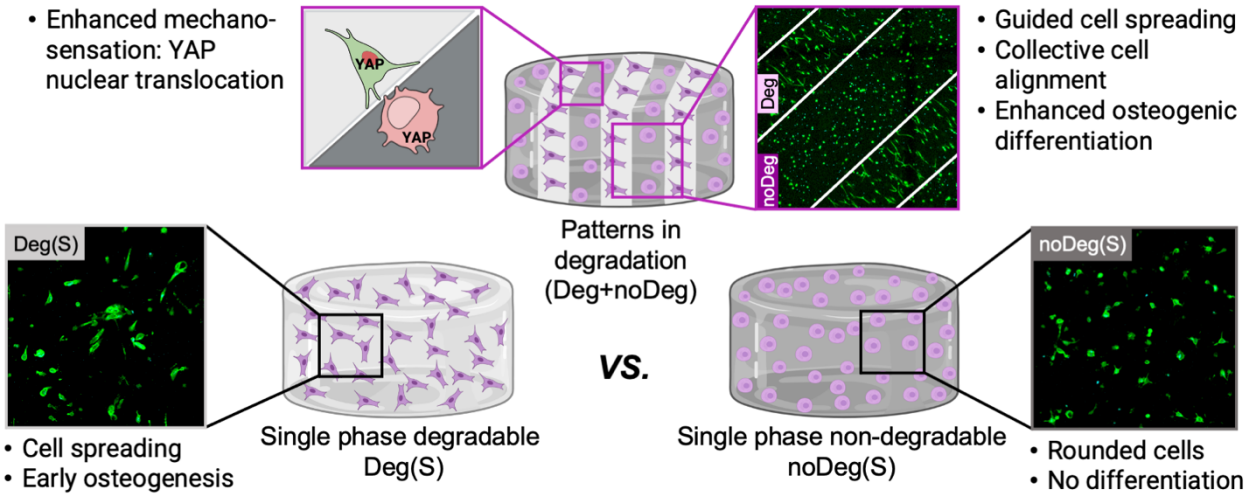

1 Introduction

Tissue engineering involves assembling cells and mimicking the complex anisotropic architecture of biological tissues to perform specific functions. The use of human mesenchymal stromal cells (hMSCs) is a promising approach in regenerative medicine [1], due to their self-renewal, clonality (proliferation from a single cell) and potency (differentiation into different cell types) [2]. Encapsulation of hMSCs in biomaterials offers a variety of options to guide and control their behavior, by modulating the local chemistry and physics provided to cells [3][4]. Hydrogels are widely used biomaterials thanks to their high cytocompatibility [5] and modifiable chemistry, providing tunable biophysical [6] and biochemical [7] properties. These have been shown to trigger specific cell activities, such as matrix stiffness [8][9][10], viscoelasticity [11] [12], degradability [13], ECM interaction by adhesion ligands [14], or ECM fiber arrangements [15]. In many cases these efforts have focused on homogeneous materials in which the cells reside. However, biomaterials in nature are typically anisotropic and provide a distinct architecture to cells.

Thus, single-phase materials can only partially provide a mimicry of the complex ECM interaction in living tissues. Native ECM is anisotropic with distinct spatially segregated properties [16]. Multiple phases in one matrix arranged in spatially discrete sections - patterned biomaterials - allow to mimic this natural ECM anisotropy, while keeping the benefits of a well-controlled synthetic material niche. The versatility of 3D patterned materials allows to tune biophysical properties and guide cell behavior. For example, patterns in biomolecule presentation have been used to spatially guide cell migration and alignment [17][18]. Despite their potential, the study of 3D patterned synthetic niches as analogs of anisotropic tissue architecture is still limited, especially how patterns in degradation can influence cell behavior. Degradable patterned microchannels have been used to guide endothelial cell sprouting [19], endothelium formation [20] and cell invasion [21] [22]. For other cell types, such as fibroblasts [23] or hMSCs [24], materials with patterns in degradation and stiffness have been studied

64 in 3D. However, the effect of patterned matrix degradation, without the influence of other
65 biophysical/biochemical factors, in controlling encapsulated cell behavior in multicompartment
66 materials has not been fully elucidated yet.

67 The mechanisms underlying cell-matrix interactions in 3D degradable materials are traction forces
68 [25] that interact with the dynamic matrix and newly opened space due to degradation [24]. It has
69 been previously shown that degradable materials favor a spread cell morphology [26] and MSC
70 osteogenic differentiation [27]. The traction forces and integrin-mediated cell interactions in
71 degradable materials are regulated through mechanosensing pathways. Yes-associated protein (YAP)
72 and transcriptional coactivator with PDZ-binding motif (TAZ) represents one of such pathways and
73 enables nuclear mediators of mechanical signals exerted by the ECM and cytoskeletal tension [28].
74 The activation of this pathway is linked to the integrins on the cell surface and the associated
75 anchoring points in the ECM (e.g. binding motifs) [29]. This, in turn, is modulated by the
76 dimensionality and the degradability of the ECM [30]. YAP/TAZ expression and nuclear
77 translocation as a consequence of cytoskeletal tension, and its effect on cell differentiation [31], cell
78 communication [32] or cell polarization through spatial heterogeneity in YAP activation [33] are well
79 known. However, the influence of multicompartment materials in YAP-mediated
80 mechanotransduction requires further research.

81 Here, we investigate how 3D patterns in alginate hydrogel degradation affect hMSC behavior and
82 how multicompartment materials differ from single-phase materials. In particular, we induce hMSC
83 spreading, collective alignment, enhanced YAP nuclear translocation and osteogenic differentiation
84 solely with anisotropic hydrogel degradation and under standard cell growth media. Such effect is
85 enhanced under osteogenic media. Additionally, we explore the mechanisms driving osteogenesis in
86 3D patterned materials, particularly YAP nuclear translocation, and show that both matrix adhesion
87 and degradation characteristics are a necessary requirement. These results advance our understanding

88 of cell response in anisotropic microenvironments. Mimicking tissue anisotropy in 3D patterned
89 hydrogels could have broad applications in biofabrication and tissue engineering.

90 2 Materials and Methods

91 2.1 Alginate modification

92 Norbornene and tetrazine were added to the alginate backbone via carbodiimide chemistry (see Fig.
93 1A and further details in Suppl. Fig. 1). The alginate used was low molecular weight, high guluronic
94 acid sodium alginate (MW 75 kDa Pronova UP VLVG; NovaMatrix). The coupling of norbornene
95 (N, TCI Chemicals, #N0907) and tetrazine (T, Conju-probe, #CP-6021) to the alginate molecule was
96 performed as previously described [23]. Alginate modification with norbornene was performed with
97 a theoretical degree of substitution (DS_{theo}) of 500. Alginate modification with tetrazine was
98 performed with a DS_{theo} of 170 (Suppl. Table S1). NMR spectroscopy was used to determine the
99 actual DS (DS_{actual}) (Suppl. Fig. S2). The quantification of the DS was performed by averaging the
100 characteristic peak area: for tetrazine 10.2, 8.2 and 7.4 ppm and for norbornene 6.2-5.8 ppm, then
101 dividing this value by the area of the characteristic alginate peak (G-1) between 5.2-4.8 ppm. NMR
102 measurements were performed, using a 1.5 % w/v alginate solution in deuterium oxide (64 scans;
103 Agilent 400 MHz Premium COMPACT equipped with Agilent OneNMR Probe) and analyzed using
104 MestreNova Software (version 12.03).

105 2.2 Isolation and culture of primary human bone-marrow derived mesenchymal stromal cells
106 (hMSCs)

107 Bone-marrow derived hMSCs (female, 50 years, no secondary diagnosis, no co-medication) were
108 received from the Core-Facility "Cell Harvesting" of the Berlin Institute of Health (BIH). The cells
109 were isolated from metaphyseal bone marrow biopsies from patients undergoing hip replacement at
110 the Charité - Universitätsmedizin Berlin, as previously described [34][35]. Written informed consent

111 was given, and ethics approval was obtained from the local ethics committee/institutional review
112 board (approval number EA2/089/20) of the Charité – Universitätsmedizin Berlin.

113 For differentiation analyses, hMSCs in passage P5 were encapsulated in hydrogels and incubated in
114 growth or osteogenic media. For further information on cell isolation and cell culture procedures,
115 please refer to Supplementary Information 1.

116 2.3 Fabrication of anisotropic matrices: 3D patterns in alginate hydrogel degradation

117 Hydrogels were fabricated based on previously established protocols [23]. The single-phase materials
118 (no photo mask) were used as controls for mechanical testing of bulk properties by rheology with a
119 frequency sweep test (Section 2.4.1), and for cell stainings. In addition, 3D patterned hydrogels were
120 generated as described below. For all material samples, cell culture was performed either in growth
121 or osteogenic.

122 2.3.1 Non-degradable matrix: Diels-Alder click-crosslinking

123 The precursors for the hydrogel were dissolved in phosphate-buffered saline (Merck #D8537) and
124 distributed into 2 tubes. The first tube contained norbornene-modified alginate (N-alg); MMP-
125 sensitive (MMPsens) peptide (GCRD-VPMS ↓ MRGG-DRCG, 95 % purity; WatsonBio) at a final
126 concentration of 5 mg/ml of hydrogel, thiolated RGD-peptide (CGGGGRGDSP; Peptide2.0) at a
127 theoretical concentration of 5 molecules of RGD per alginate chain (DS 5, 1.2×10^{-3} mM), and the cell
128 suspension at final concentration of 2×10^{6} cells/mL of hydrogel. The second tube contained tetrazine-
129 modified alginate (T-alg) and the photoinitiator (Irgacure 2959; Sigma-Aldrich, #410896) at a final
130 concentration of 3 mg/mL of hydrogel. The total final concentration of alginate was 2 % w/v at a N:T
131 ratio of 1.5. Despite MMPsens and the photoinitiator being present, these were not activated due to
132 the lack of UV exposure. Nevertheless, the MMPsens and photoinitiator need to be present to allow
133 for patterned materials (see Section 2.3.3).

134 The two solutions were mixed by pipetting and cast onto a bottom glass plate (borosilicate glass,
135 Filafarm, #1000185), with the casting area being restricted on three sides by glass spacers
136 (Marienfield, #1100420), and immediately covered with a glass slide previously treated with
137 SigmaCoat (≥ 99.5 %; Sigma-Aldrich, #SL2) to prevent adhesion. The gel height was constrained to
138 2 mm by the thickness of the glass spacers. Spontaneous click-crosslinking for 60 min at room
139 temperature (RT) and in the dark allowed Diels-Alder crosslinking and the N:T covalent bonds to
140 form (Fig. 1B).

141 In order to ensure a homogeneous binding of the RGD-peptide, crosslinked gels were subsequently
142 exposed to 2 min UV light (365 nm) at 10 mW/cm^2 (Omnicure S2000) in a custom-built exposure
143 chamber. The RGD-peptide binds to the free norbornenes via thiol-ene reaction (Fig. 1C). The
144 cylindrical hydrogels were punched from the cast gel sheet using 5 mm biopsy punches (Integra
145 Miltex) and incubated in cell culture media at 37 °C and 5 % CO_2. Further information on the
146 reaction timeline can be found in Fig. 1E.

147 **2.3.2 Degradable matrix: UV-mediated thiol-ene crosslinking with MMPsens peptide**

148 The production of degradable materials followed the same procedure as described in Section 2.3.1,
149 with an additional step for the MMPsens peptide crosslinking. After casting the hydrogel solution
150 between the glass plates, the material was immediately exposed to UV light at 10 mW/cm^2 for 10
151 min to initiate the coupling of the degradable MMPsens peptide to the norbornene-modified alginate
152 via thiol-ene crosslinking (Fig. 1D). After the UV exposure, the materials were placed for an
153 additional 50 min at RT in the dark to allow for the N:T covalent bonds to be formed. To ensure a
154 homogenous binding of RGD, the hydrogels were finally exposed again to UV for 2 min (Fig. 1C).
155 Further information on the reaction timeline can be found in Fig. 1E. Hydrogels were punched out
156 and incubated in cell culture media at 37 °C and 5 % CO_2.

157 The mechanical properties (measurement method described in Section 2.4) can be modulated by
158 varying the concentration of MMPsens peptide (Fig. 1F) and by tuning the N:T ratio (Fig. 1G). For a
159 constant N:T ratio of 1.5, the non-UV exposed noDeg regions have a constant elastic modulus, while
160 the UV exposed Deg regions results in stiffer matrices with increasing MMPsens peptide
161 concentration (Fig. 1F). In contrast, for constant MMPsens peptide concentration of 5 mg/mL, the
162 non-UV exposed noDeg regions have a decreasing elastic modulus with increasing N:T ratio, while
163 the UV exposed Deg regions results in stiffer matrices with increasing N:T ratio, due to the greater
164 abundance of N-alg available for the thiol-ene crosslinking (Fig. 1G)

165 **2.3.3 Anisotropic matrix: Photolithography of patterned dual crosslinked hydrogels**

166 The creation of patterned materials followed the same procedure as described in Section 2.3.2, with
167 the addition of a photomask placed on top of the cover glass during the UV mediated thiol-ene
168 coupling of the MMPsens peptide. The photomask had a pattern of straight lines with 500 µm
169 thickness (UV light blocking sections, non-degradable matrix equivalent to 2.3.1) placed 300 µm,
170 500 µm or 800 µm apart (UV light permitting sections, degradable matrix equivalent to 2.3.2). After
171 the 10 min UV exposure through the photomask, followed by 50 min incubation in the dark at RT, in
172 which all the N-T bonds were formed and no additional grafting of MMP occurred, crosslinked gels
173 were exposed to 2 min UV light at 10 mW/cm^2 without a photomask for homogeneous binding of the
174 RGD-peptide (Fig. 1E).

175 Two additional control materials are included in this manuscript: materials with a non-degradable
176 peptide sequence and materials with no RGD adhesion peptide. The control materials with a non-
177 degradable peptide sequence were achieved by replacing the MMPsens with the homologous
178 scramble (MMPscr) peptide (GCRD-VpMS ↓ mRGG-DRCG, 95 % purity; WatsonBio), where the
179 amino acids in lower case were switched for the D-isoform, unrecognizable by MMP enzymes. For

180 the control materials with no adhesion peptides, the thiolated RGD solution was replaced with PBS.
181 All of the controls follow the procedure established under section 2.3.3.

182 2.4 Hydrogel mechanical characterization over time

183 Mechanical characterization was performed on day 1 and day 14. All mechanical characterization
184 was performed with cell-laden materials to quantify the effect of cell-driven enzymatic degradation
185 of the hydrogels. The material degradation and changes in mechanical properties were evaluated via
186 two different methods: (i) rheology with a frequency sweep test to measure the bulk shear modulus,
187 *G* (and then calculate the elastic modulus, *E*), (ii) microindentation to measure the surface elastic
188 modulus of single-phase and patterned materials, and display the iso- or anisotropic values with a
189 surface map.

190 2.4.1 Rheology

191 Storage and loss modulus of single-phase hydrogels were determined with a rheometer (Anton Paar
192 MCR301) via frequency sweeps with a parallel plate geometry of 8 mm (PP08, Anton Paar). The
193 frequency sweep was performed from 0.01 to 10 Hz and at 0.1 % shear strain at RT (n = 6). Once
194 contact with the gel surface was established, a pre-compression of 10 % of the height of the hydrogel
195 was applied prior to the measurement. No additional hydration was needed as the experiment lasted
196 less than 10 min. To obtain the elastic modulus, first the shear modulus (G) was derived from the
197 storage (G') and loss (G") modulus using Rubber's elasticity theory $G = \sqrt{G'^2 + G''^2}$ [36]. The
198 elastic modulus (E) was calculated using the values of *G* and the approximation of Poisson's ratio (ϑ)
199 equal to 0.5, $E = 2G\ (1 + \vartheta)$ [37]. The mesh size (ξ) was approximated based on storage modulus
200 G' in low frequencies (0.1-1Hz), $\xi = \sqrt[3]{6RT/G'\pi\ N_{av}}$, as previously described [38].

201 **2.4.2 Microindentation**

202 To verify the emerging patterns in mechanical properties of the 3D hydrogels due to anisotropic
203 degradation, the surface elastic modulus of the materials on day 1 and day 14 was mapped into a
204 heatmap. Depth-sensing microindentation measurements were done using a Triboindenter TI-950
205 (Hysitron-Bruker, MN, USA) with a cono-spherical tip of 50 µm radius. The tip was calibrated by an
206 air indent, followed by a quick approach to detect the surface. Similar procedures as previously
207 described were used [23], but were adapted for softer materials. Then, the measurements were
208 automatized as follows: ~350 µm retraction, an indent approach of ~150 µm and strain rate of ~30
209 µm/s. The measurements were done in automated mode to map a 2 x 2 mm^2 area with 10 x 10
210 indents and 200 µm spacing. To ensure that the sample remained hydrated during the measurement,
211 the samples were fixed to a sponge and partially submerged in PBS.

212 To obtain the elastic modulus from the load-displacement indentation curves, the Hertzian contact
213 model was used. The analysis of the load-displacement curves was automated by a custom-made
214 Python3 script. We used an adapted version of the script described in our previous work [23], related
215 to the selection of the origin point. The origin point is the initial contact point where the tip gets in
216 contact with the material surface and from which the Hertzian model will be determined. This
217 procedure was previously automatized by mathematically determining the minimum of the first part
218 of the indentation curve. However, in very soft materials like the ones presented in this study, the
219 origin point could not be identified using the previous method, as the initial contact point was not as
220 clear as with stiffer gels. The adapted version of the script allows the user to select the origin point
221 manually.

222 **2.5 Characterizing volume and wet weight changes over time**

223 To track the degradation of single-phase materials, volume changes, wet weight changes and swelling
224 ratios (S_t) were tracked over time, at 0 (after 2 h equilibration), 1, 3, 5, 7, 14, 21 and 28 days. At each
225 time point, single-phase hydrogels were weighed under sterile conditions and measured using a
226 caliper. The volume was determined assuming a cylindrical shape, calculated from one height
227 measurement and the mean of two diameter measurements. Swelling (S) was calculated with the
228 equation $S_t=W_t/W_{t=0}$, where W_t refers to the hydrogel wet weight at a given time point t, and $W_{t=0}$
229 refers to the hydrogel wet weight at the initial time point.

230 **2.6 Primary hMSC viability and cell number**

231 To verify cell viability Live/Dead stainings were performed after 1 and 14 days. The hydrogels were
232 taken out from the incubation media and washed with PBS (Merck #D8537). Then the cells were
233 stained with a solution of 4 µM Calcein AM (Biomol Bioquest #ABD-22002, 500x solution in
234 DMSO) and 4 µM Ethidium homodimer-1 (Sigma #E1903, dilution 1:1000 from original solution)
235 dissolved in PBS to identify live and dead cells, respectively. The staining solution volume was 400
236 µl per hydrogel in a 24 well plate, stained for 12 min in a cell culture incubator at 37 °C, 5 % CO_2 in
237 the dark. A final washing step was performed with 400 µl of PBS per hydrogel at RT for 5 min and
238 protected from light.

239 Imaging was performed on a confocal microscope (Leica SP5, Germany). Quantification of cell
240 number and viability at each time point was performed using ImageJ software (ImageJ 1.53s) [39].
241 One position from 3 independent samples was acquired at the gel center at 10x water-immersed
242 objective (HCX APO L U-V-I 10.0x 0.30), with tile merging of 3x3 and a 250 µm z-stack.

243 **2.7 Primary hMSC morphology**

244 Cell morphology was assessed after 1 and 14 days, staining the nuclei and actin cytoskeleton using
245 SYTOX and Phalloidin, respectively. All steps were performed under orbital shaking in a 24 well
246 plate and using a volume of 500 µL per gel. The culture media was removed and the gels were
247 washed twice with PBS (Merck #D8537). Then, the encapsulated cells were fixed in 4 %
248 paraformaldehyde solution (Sigma-Aldrich, #158127) for 45 min at RT, followed by
249 permeabilization with 0.3 % Triton X-100 (Sigma-Aldrich, #11488696) for 15 min, washed twice
250 with 3 % bovine serum albumin (BSA, Sigma-Aldrich, #A7906) in PBS for 5 min. The staining
251 solution was dissolved in PBS containing 0.1 % TritonX-100 and 3 % BSA and with the following
252 concentrations: 0.5 µM SYTOX (Thermo Fisher, #S11381) and 1 µg/mL of Phalloidin 405
253 Conjugate (CruzFluor™, #SC363790). The staining was performed protected from light, during 4 h
254 at RT. Final washing was performed twice with 3 % BSA in PBS for 5 min at RT.

255 For imaging, three different positions per gel were acquired at the gel center from two independent
256 samples using a confocal microscope (Leica SP5, Germany). For a general quantification of cell
257 morphology, 10x water-immersed objective (HCX APO L U-V-I 10.0x0.30), with a tile merging of
258 2x2 was used and a 250 µm z-stack.

259 **2.8 Primary hMSC differentiation**

260 Cell differentiation was tested using Osterix (OSX) as an early osteogenic differentiation (see section
261 2.9), Osteocalcin (OCN) as medium osteogenic differentiation (see section 2.9), and OsteoImage as
262 late osteogenic differentiation marker. The stainings were performed after 14 days, always in
263 combination with cell morphology staining, SYTOX and Phalloidin, as described in Section 2.7.

264 For OsteoImage (Lonza, #PA1503) the staining procedure followed the provider´s instructions.
265 Briefly, the fixed cells (see section 2.7) were washed with the wash buffer twice for 5 min. Then, the
266 previously diluted 1:100 Osteoimage staining reagent in dilution buffer was added to the gels, 500 µL

267 per gel. The incubation was carried out at 4 °C, overnight and protected from light. The next day, the
268 samples were washed three times with the wash buffer and then imaged.

269 For imaging, three different positions per gel were acquired at the gel center from two independent
270 samples using a confocal microscope (Leica SP5, Germany). For a higher magnification
271 quantification of cell morphology, 25x water-immersed objective (HCX IRAPO L 25.0x0.95), with a
272 tile merging of 4x4 was used and a 250 µm z-stack.

273 **2.9 Immunostainings**

274 YAP, Osterix (OSX) and Osteocalcin (OCN) expression was evaluated by immunofluorescence.
275 After performing the morphological staining, SYTOX and Phalloidin, as described in Section 2.7, the
276 primary antibody was incubated for 24 h at 4 ºC under constant rocking. The antibodies used were:
277 YAP IgG2aκ mouse monoclonal (Santa Cruz, #sc-101199) at 10 µg/mL in PBS, OSX polyclonal
278 rabbit (abcam, ab22552) 10 µg/mL in PBS-1%BSA and OCN monoclonal mouse IgG1 (R&D
279 Systems, #MAB1419) at 25 µg/mL in PBS. After the primary antibody staining, the samples were
280 washed three times with 400 µL of 3 % BSA in PBS for 30 min. The secondary antibody
281 (ThermoFisher, #A32728) was stained for 2 h at RT under constant rocking. Finally, the samples
282 were washed 3 times with 3 % BSA in PBS and imaged.

283 For imaging, three independent positions per gel were acquired at the gel center from two
284 independent samples using a confocal microscope (Leica SP5, Germany). For a higher magnification
285 quantification of cell morphology, 25x water-immersed objective (HCX IRAPO L 25.0x0.95), with a
286 tile merging of 4x4 was used and a z-stack of 250 µm.

287 **2.10 Quantitative analysis of stained sections**

288 The cell morphology in 3D patterned materials was evaluated using a previously described macro
289 [23] written in ImageJ (ImageJ 1.53s, [39]). The cell projected area, cell circularity and cell number
290 were obtained from z-stack projections. The macro offers the possibility to freely divide an image
291 into a grid, which leads to a heat map in which the results are later depicted. The cell border threshold
292 was manually set.

293 To evaluate collective cell alignment, the Image J plugin Directionality was used [40]. The graphs
294 show the 'Direction (°)' or angle vs. the 'Amount', which shows the fraction of cells with a preferred
295 direction, normalized to the total cell number.

296 YAP, Osterix (OSX) and Osteocalcin (OCN) expression was quantified as a percentage of the marker
297 expressing cells (YAP, OSX or OCN or positive cells) divided by the total cell number (SYTOX).
298 The images were evaluated using ImageJ: first, a background subtraction of a control image of the
299 staining with only the secondary antibody was performed, followed by setting manually the threshold
300 and finally evaluating with the automatic particle counting function. The mineralized area obtained
301 with OsteoImage (OI) staining, was established as a percentage by dividing the OI positive cell area
302 by the total cell area (phalloidin staining).

303 The nuclear to cytoplasmic ratio of YAP was evaluated using a previously described method [41].
304 Briefly, individual cells were segmented for nucleus (SYTOX) and cytoplasm (phalloidin) to define
305 the respective subcellular regions. Next, YAP average intensity within each subcellular region was
306 quantified and the ratio calculated.

307 **2.11 Flow cytometry analysis**

308 After 14 days of encapsulation, the cells were retrieved from the hydrogels using alginate lyase
309 (Sigma, #A1603, reconstituted in Ca/Mg-free PBS in 2mg/mL). The cells were incubated for 30 min

310 at 37C, then centrifuged at 400 rcf during 5 min and washed twice with PBS. The flow cytometry
311 staining and analysis was done as described before [42]. The viable cells were determined using
312 fixable live/dead blue staining kit for UV excitation (Thermo Fisher L34962). The blocking solution
313 (FcX, BioLegend, 422301) was used to prevent unspecific binding. Staining with antibodies
314 (Supplementary table 2) was performed on ice and using flow cytometry buffer (phosphate-buffered
315 saline (PBS) including bovine serum albumin (0.5% w/v) and sodium acid (0.1% w/v)). Fixation and
316 permeabilization kit (BioLegend, 426803) was used for intracellular staining. The stained cells were
317 analyzed on an ID7000 spectral flow cytometry (Sony Biotechnology, San Jose, CA, USA) with
318 individual autofluorescence unmixing. Gating and analysis of the population were performed with
319 FlowJo software (Tree Star, USA), further analysis were performed in R Statistical Software (v4.4.1;
320 R Core Team 2024) using the Spectre packages [43].

321 **2.12 Statistical analysis**

322 Statistical analysis was performed with GraphPad Prism 8 (version 8.4.3 for Windows, GraphPad
323 Software Inc., Boston, Massachusetts USA). To test for normality, the Shapiro-Wilk test was applied.
324 For normally distributed data, bar plots showing mean and standard deviation (SD) were used and the
325 statistical comparison was performed using ANOVA (* alpha < 0.05, ** alpha<0.01 or ***
326 alpha<0.001), corrected with Bonferroni test for multiple comparisons. For not normally distributed
327 data, box plots with median, 1st and 3rd quartile were used and data was compared using a Kruskal-
328 Wallis test (* alpha < 0.05, ** alpha<0.01 or *** alpha<0.001), corrected with Dunn´s test for
329 multiple comparisons

330 **3 Results**

331 **3.1 Anisotropic degradation of cell-laden patterned hydrogels leads to emerging patterns in**
332 **mechanics**

333 Cells were encapsulated in photopatterned alginate hydrogels (Fig. 2A) with initial homogeneous
334 mechanical properties (Fig. 2J). The comparable mechanical characteristics of the materials were
335 achieved by tuning the MMPsens peptide concentration (Fig. 1F) and the N:T ratios (Fig 1G). The
336 mechanical properties of cell-laden hydrogels evolved during time due to the cellular enzymatic
337 action (Fig. 2A). Those mechanical properties were characterized by rheology (Fig. 2B, C, D, G) and
338 microindentation (Fig. 2H-J).

339 The degradable and non-degradable materials have comparable values of loss (G′) and storage (G′′)
340 modulus on day 1 (Fig. 2B). However, on day 14 there is a pronounced difference in G′ and G′′ for
341 Deg materials (Fig. 2C). A significant decrease over time in mechanical properties of Deg materials
342 is observed, whereas the noDeg materials preserve their elastic modulus (Fig. 2D). The elastic
343 modulus on day 1 of Deg (2.07 ± 0.28 kPa) is comparable to noDeg (2.03 ± 0.22 kPa). Significant
344 differences can be seen between the elastic modulus of Deg (0.39 ± 0.27 kPa) and noDeg (1.87 ±
345 0.38 kPa) on day 14. The elastic modulus changes can be related to the water content as there is a
346 significant difference in the swelling (Fig. 2E) and volume changes over time (Fig. 2F), which is also
347 reflected in an increasing mesh size (Fig. 2G). The swelling and volume of Deg gels starts to
348 decrease after 5 days due to degradation, while a less dynamic behaviour is seen in the noDeg
349 materials. The mesh size of Deg materials increases significantly between day 1 (24 ± 1 nm) and day
350 14 (59 ± 5 nm), whereas in noDeg materials the mesh size remains unchanged from day 1 (21 ± 0.3
351 nm) to day 14 (22 ± 1 nm).

352 Compared to the degradation behavior of single-phase materials, the corresponding phases in
353 patterned materials show similar characteristics, as shown by the average surface elastic modulus of
354 microindentation measurements (Fig. 2J). As seen in the representative surface map of elastic
355 modulus, the pattern in degradation emerges over time. There is no distinct pattern of the surface
356 elastic modulus on day 1 (Fig. 2H), with values fluctuating around 2.5 kPa, consistent with the

357 comparable bulk elastic modulus of both single-phase materials (Fig. 2D). However, on day 14 (Fig.
358 2I), there are softer sections (1-1.5 kPa) corresponding to the Deg zones and stiffer sections (2.5 kPa)
359 associated with noDeg zones.

360 **3.2 Anisotropic hMSC morphology and collective cell alignment in 3D patterned materials**
361 **compared to single-phase counterparts**

362 hMSCs were encapsulated in 3D anisotropic materials with patterns in degradation. The viability and
363 cell number were evaluated using Calcein/ EtHD1 staining. Cell viability (fraction of Calcein (+)
364 cells) remained high on day 1 (Suppl. Fig. S3A-B) and day 14 (Suppl. Fig. S3D-E) and there were no
365 visible patterns in cell viability. Cell proliferation was also evaluated by individual quantification of
366 the average cell number (total cells, Calcein and EtHD1) (Suppl. Fig. S3C and S3F).

367 Next, we investigated the effect of patterned hydrogels on cell morphology and collective alignment.
368 Patterned materials with dimensions of 500 µm:500 µm for Deg:noDeg (Fig. 3A) were compared on
369 day 14 to single-phase materials (Fig. 3E, 3G). On day 1 (Suppl. Fig. S4A-C), cell morphology was
370 similar among the two phases of the patterned material, not showing any significant differences,
371 neither in projected cell area (Fig. 3H) nor in circularity (Fig 3I). Patterns in cell morphology were
372 visible on day 14 (Fig. 3A) and were quantified through heatmaps (Fig 3B-C). The results showed
373 increased projected cell area (Fig. 3B) and decreased circularity (Fig. 3C) in Deg regions, while cells
374 remained round and with smaller projected cell area in noDeg zones. Similar trends were observed in
375 equivalent single-phase materials (Fig. 3D-G). However, the effect in the morphological changes was
376 significantly enhanced in the Deg sections of patterned materials in contrast to the single-phase Deg
377 (Fig. 3H-I).

378 The patterned materials allowed enhanced changes in cell morphology but also differences in
379 collective cell alignment (Fig. 4). The cell orientation was evaluated for patterns of different

380 Deg:noDeg dimensions, 300 μm:300 μm (Fig. 4A-C), 500 μm:500 μm (Fig. 4D-F) and 800 μm:200
381 μm (Fig. 4G-I). The 300 μm:300 μm photomask (Fig 4A) resulted in cells collectively aligned
382 perpendicular to the stripes in the Deg phases (Fig 4B), in contrast to the cells in noDeg sections (Fig
383 4C), where cells remained round and had no predominant orientation. This effect was further
384 enhanced with the 500 μm:500 μm photomask (Fig. 4D-F). However, for the 800 μm:200 μm
385 photomask (Fig 4G), with a broader degradable section, the collective cell alignment was lost (Fig.
386 4H) and was equivalent to single-phase materials (Suppl. Fig. 5A-D), where we found a spread cell
387 morphology but lacked a collective cell alignment. Similarly, no collective alignment was found in
388 patterned materials when subjected to constrained swelling in the XY direction (Suppl.Fig.5E-L).

389 **3.3 Enhanced and spatially guided hMSC osteogenic differentiation in 3D patterned**
390 **materials compared to single-phase counterparts**

391 In the previous sections we showed that 3D patterns in alginate hydrogel degradation induced an
392 anisotropic response in hMSC morphology and emergent properties such as collective cell alignment.
393 This motivated further investigation of the anisotropic hMSC osteogenic differentiation, evaluated by
394 early (Osterix, OSX) and intermediate (Osteocalcin, OCN) osteogenic markers.

395 The anisotropic biophysical cues provided by the patterned materials already induced significantly
396 enhanced and spatially segregated osteogenic differentiation of hMSC over 14 days in growth media
397 (Fig. 5). The early osteogenic marker OSX (Fig 5A-C) was expressed in the Deg single-phase
398 materials (Fig. 5B) and also in the Deg phase of patterned materials (Fig. 5A), though to a lower
399 extent (Fig. 5G). Furthermore, the intermediate osteogenic marker OCN, indicative of further
400 differentiated hMSCs, was significantly higher (Fig. 5H) in the Deg sections of patterned materials
401 (Fig 5D) compared to single-phase Deg materials (Fig. 5E). The noDeg phases in both patterned and
402 single-phase materials (Fig. 5C, F) did not allow osteogenic differentiation of hMSCs.

403 With flow cytometry, individual cells can be explored on a higher parametric level. Cells were
404 retrieved from three different types of hydrogels: single-phase degradable (Deg(S)), single-phase
405 non-degradable (noDeg(S)), and patterned 3D hydrogels (patterned), after culturing for 14 days. We
406 investigated the changes in cell phenotype by analyzing various cell surface markers, as well as
407 intracellular markers, allowing to trace the differentiation from stem-like characteristics towards
408 osteogenic cells (Fig. 6). Dimension reduction (UMAP) of all cells from the three groups showed
409 distinct clustering of the groups (Fig 6A-G). The mean fluorescence intensity (geometric MFI)
410 allowed to determine the expression level of measured markers. All retrieved cells from the 3D
411 materials were negative for the markers CD45, CD34, CD166, CD271 and CD146. The surface
412 markers CD90, CD105, CD73, considered as minimal criteria for hMSC, showed altered positive
413 expression levels with CD90 (Fig 6H), especially, being higher expressed in the degradable
414 compared to the noDeg material (Fig 6H, K).

415 The intracellular markers Osteocalcin (OCN), Alkaline Phosphatase (ALP) and Osteopontin (OPN)
416 allowed to trace the osteogenic differentiation of encapsulated hMSCs, which show an increased z-
417 score of OCN and ALP in Deg materials (Fig. 6I, K). Interestingly, a small subset of cells in the
418 noDeg material expressed higher levels of OPN (Fig 6J, K).

419 To evaluate the difference between the patterned and single-phase materials, a principal component
420 analysis was performed (Fig 6L). The x-axis represents Principal Component 1 (PC1), which
421 explains 45.3% of the variance, while the y-axis represents Principal Component 2 (PC2), capturing
422 18.7% of the variance. Despite the overlap between the groups, the trend shows 3 distinct groups
423 enclosed in a 90% CI ellipse with an overall 64% explained variances. This indicates that the
424 patterned material induced a distinct cellular composition that differs from the respective single-
425 phase materials.

426 **3.4 Enhanced and spatially guided mechanosensing via YAP/TAZ signaling in 3D patterned**
427 **materials compared to single-phase counterparts**

428 After establishing the significant differences in patterned hMSC projected cell area, circularity,
429 collective cell alignment and osteogenic differentiation, we investigated the underlying mechanism.
430 Based on the observation of morphological changes and associated cytoskeletal tension in degradable
431 regions, we investigated YAP positive expression (YAP(+)) as a binary measurement, independent of
432 intensity, as well as its nuclear to cytoplasmic localization within single cells in patterned materials
433 (Fig. 7A-C) and compared it to the single-phase counterparts (Fig 7D-G).

434 The fraction of YAP(+) cells was significantly higher in Deg materials patterned (Fig 7A) and single-
435 phase (Fig 7D) compared to noDeg (Fig. 7E) on day 14 (Fig 7H). Independent of the material or the
436 patterning, the YAP expression was equally distributed over the nucleus and the cytoplasm on day 1
437 (Fig 7I). On day 14, there was a nuclear translocation (nuc./cyto. >1) in Deg materials, patterned (Fig
438 7B) and single-phase Deg (Fig 7F), whereas for the noDeg materials, in patterned (Fig 7C) and in
439 single-phase (Fig 7G), it remained close to 1. The effect of nuclear YAP translocation was
440 significantly higher in Deg phases of patterned materials compared to Deg phases in single-phase
441 materials (Fig. 7I).

442 To test the influence of degradation in the YAP translocation, the MMPsens peptide crosslinker was
443 replaced with the homologous non-degradable scramble peptide (MMPscr). The MMPscr allowed the
444 comparison of the degradable and non-degradable material with the same chemical crosslinking and
445 mechanical properties (ex. crosslinker length). The MMPscr patterned materials showed a very
446 similar behavior on day 1 (data not shown) compared to day 14 (Fig. 7J-L). The lack of degradation
447 in the MMPscr regions led to a rounded cell morphology with a similar YAP expression (Fig. 7J-K)
448 as the one seen in noDeg phases (Fig. 7G). Both phases with MMPscr and noDeg patterned materials

449 had a similar YAP (+) cell percentage (Fig. 7M) and YAP localization (Fig. 7N), with no significant
450 differences neither between phases nor over time.

451 To test the relevance of integrin activation and cell-matrix interaction with alginate, we used
452 materials lacking RGD adhesion peptides (Fig. 7O-S). The cells in noRGD patterned materials
453 showed a similar behavior in the two phases on day 1 (data not shown) as well as on day14 (Fig 7O-
454 Q). The fraction of YAP(+) cells was lower (Fig. 7R) compared to materials with RGD (Fig. 7H).
455 Moreover, there were no significant differences in YAP(+) cells (Fig 7R) or localization (Fig. 7S),
456 neither between phases nor over time.

457 **3.5 Additional biochemical stimuli can enhance the spatially guided hMSC osteogenic**
458 **differentiation**

459 hMSC differentiation was further tested under osteogenic media to evaluate the effect of biochemical
460 stimuli in patterned materials. Cell morphology patterns are enhanced with osteogenic media (Fig.
461 8A-E) when compared to growth media (Fig. 3A), showing larger projected cell area (Fig. 8B) and
462 elongated cells with lower circularity (Fig. 8C) in Deg regions.

463 The intermediate osteogenic marker OCN had higher expression in osteogenic media (Fig. 8F)
464 compared to growth media and shows a significantly higher expression in Deg phases compared to
465 noDeg phases (Fig. 8F, K). Despite the biochemical stimuli of osteogenic media, the restrictive
466 environment of noDeg sections resulted in only a low number of OCN positive cells (Fig 8K). The
467 late osteogenic marker (mineralization, OsteoImage) (Fig. 8G, L) also had higher expression in
468 osteogenic media compared to growth media, with significantly higher mineralized area in Deg
469 sections compared to noDeg sections (Fig. 8L).

470 The fraction of YAP(+) cells in osteogenic media (Fig. 8H) showed also increased expression on day
471 14 in the Deg regions, but with overall increased values compared to growth media (Fig. 5M). The

472 YAP nuclear to cytoplasmic ratio shows a similar significant pattern over time in osteogenic media
473 compared to growth media (Fig. 8N), with nuclear translocation in the Deg phase (Fig. 8I) and
474 cytoplasmic expression in the noDeg phase (Fig. 8J). In the Deg phase the use of osteogenic media
475 significantly enhanced the nuclear translocation compared to growth media (Fig. 8M, N).

476 **4 Discussion**

477 Degradation patterned materials enhance encapsulated hMSC spread morphology, allow collective
478 cell alignment, stimulate mechanotransduction and promote osteogenic differentiation, when
479 compared to single phase materials. By investigating patterned hydrogels as opposed to equivalent
480 single-phase matrices, we aimed to highlight the importance of using multicompartment materials in
481 biomaterial design. In addition, the patterned materials with anisotropic hydrogel degradation
482 allowed elucidating the role of degradation, without additional biophysical (such as stiffness) or
483 biochemical (such as osteogenic media) cues. Our findings offer insights into how these anisotropic
484 materials influence cell response, potentially leading to better strategies mimicking tissue anisotropy,
485 with applications in biofabrication and tissue engineering.

486 The anisotropic alginate-based hydrogels used in this research consist of two soft (<3kPa) 3D
487 microenvironments for cells, with comparable initial elastic modulus at day 1, and emerging patterns
488 through degradation over time. The comparable initial elastic modulus of both phases allows a direct
489 comparison on degradability effects, excluding other biophysical properties (i.e. matrix stiffness),
490 which have already been studied [44][24]. Moreover, the combination of both matrices in a patterned
491 multicomponent material results in a structural advantage over time, as the single phase Deg
492 materials crumble and start disintegrating due to degradation, while patterned materials keep their
493 shape after 14 days (Suppl. Fig. S6). It is important to highlight the tuneability of the matrix platform
494 used, which allows different combinations of mechanical and degradation properties (Fig. 1F-G).
495 Interestingly, the click reaction described in Fig. 1G shows a maximum elastic modulus at N:T ratio

496 0.5. This is consistent with the description of an unexpected dimer formation, following a 1:2 (N:T)
497 stoichiometry [45].

498 Cell spreading is dependent on the matrix degradation and this is enhanced in Deg sections of
499 patterned materials compared to single phase counterparts. Changes in morphology are a result of the
500 remodeling of the immediate environment [30] and consistently described in MMP-sensitive peptide
501 crosslinked materials [46]. Our research showed that the interphases of the patterned materials not
502 only lead to spatially segregated cell morphology, but also influence the collective cell alignment
503 perpendicular to the stripe main axis. Cell alignment in patterned materials has been previously
504 described on 2D topographical directed patterns [47][48][49] and in 2D mesh scaffolds [50],
505 exhibiting a parallel alignment to the groves/ridges, or perpendicular to them in wider curvatures
506 (>1000 μm) [51]. However, less is known about the mechanism for collective cell alignment within
507 3D matrices. Previous studies report the perpendicular cell alignment to be a result of force and
508 neighboring tensile stress [52]. Our research showed that cell alignment is dependent on the stripe
509 dimensions (Fig 4, broader stripes show no alignment), patterning (Suppl. Fig S5, single phase
510 hydrogels show no collective alignment) and, probably, on the material´s differential swelling
511 properties (Suppl. Fig S5, constrained swelling show no alignment). The direct transfer of
512 mechanisms of collective cell alignment into 3D matrices is still at early stage, as 3D environments
513 offer multiple factors that can influence cell, such as mechanical properties, adhesive ligand
514 concentration, crosslink type and density. Yet, understanding and guiding collective cell alignment
515 will be important for developing functional biomaterials that mimic biological anisotropic tissues,
516 which rely on fiber/cell directionality for optimal performance [53].

517 The 3D patterns in hydrogel degradation allowed spatially guided hMSC differentiation, promoting
518 enhanced osteogenic differentiation in the Deg region compared to the noDeg, or single-phase
519 degradable materials in growth media (Fig. 5). Strikingly, an early osteogenesis stage as shown by

520 OSX expression could be promoted solely by biophysical factors after 14 day culture in growth
521 media (hMSCs in Deg single-phase materials, Fig. 5B). This effect was enhanced in patterned
522 materials, which at the same time point showed OCN expression, an intermediate osteogenic marker
523 (Fig 5D). Our findings agree with previous studies on stiffness-degradation 3D patterned materials
524 showing that soft and Deg matrices foster osteogenesis [24]. Our study highlights the importance of
525 matrix degradability for osteogenesis, and the potential of using patterned materials for enhancing
526 and guiding osteogenic differentiation.

527 Moreover, biochemical factors (osteogenic media) in combination with patterned materials, enabled
528 late osteogenesis and mineralization in Deg phases. Notably, mineralization within the Deg phases
529 was only observed under osteogenic media, consistent with studies showing that biomineralization is
530 a complex process [54]. Despite the biochemical cues from osteogenic media were available for cells
531 in both Deg and noDeg phases of the patterned material, the guidance of the patterns is evident with
532 broader cell spreading, higher osteogenic differentiation and increased YAP nuclear translocation in
533 the Deg phases compared to the noDeg regions. These findings highlight the interplay between
534 biochemical and biophysical cues modulating cell behavior and the synergistic effect by anisotropic
535 patterned hydrogels.

536 Further flow cytometry analysis of hMSCs encapsulated in hydrogels enabled us to identify changes
537 in cell phenotype between the materials. The density plots showed clearly distinct clustering behavior
538 of the Deg and noDeg single-phase materials (Fig 6B, C), however the patterned material did not
539 cluster along the two single-phase materials (Fig 6D, G), hinting towards distinct processes in
540 anisotropic materials and not only replicating the two individual isotropic materials. All cells were
541 consistent with the minimal criteria markers: negative for CD45, CD34, , and positive for CD90,
542 CD73, CD105 [55]. There were no hMSCs subpopulations identified as the cells were negative for
543 CD166, CD271 and CD146 [56]. Deg materials led to the upregulation of CD90 (Fig. 6H), which

544 controls vital cellular processes, including cell–cell and cell–matrix interactions, cell adhesion and
545 cell response to dynamic matrices [57][58]. Notably, CD73 shows a downregulation in the patterned
546 materials when compared to Deg and noDeg. This effect could be due to the additional mechanical
547 strain from the anisotropic material interfaces, as previous studies have shown that CD73 is
548 downregulated in mechanically loaded cells [59].

549 The intracellular markers Osteocalcin (OCN), Alkaline Phosphatase (ALP) and Osteopontin (OPN)
550 allowed to trace the osteogenic differentiation of encapsulated hMSCs. In accordance with the
551 immunofluorescence staining for Osteocalcin (Fig 5), Deg and patterned materials induced
552 osteogenic differentiation in the encapsulated cells, as shown by the increased OCN expression (Fig
553 6 I, J) compared to noDeg. It is important to highlight that the patterned materials were analyzed as a
554 bulk (Deg+noDeg regions), therefore the enhanced effects in patterned Deg phase were not captured
555 using this method. This is a limitation of bulk analyses using flow cytometry, as opposed to image-
556 based methods and immunofluorescence. Further bulk analyses of cell phenotype, such as RNA seq,
557 were no longer considered, as they would have the same limitations with patterned samples.

558 Interestingly a small subset of cells in the noDeg material expressed higher levels of OPN (Fig 6 J).
559 OPN is a multifunctional protein, which has a role in inflammatory processes [60]. Non-degradable
560 alginate-based matrices have been previously reported to upregulate differentially expressed genes
561 involved in inflammatory response in breast cancer cells [61].

562 YAP nuclear translocation and mechanotransduction is enhanced in Deg sections of patterned
563 materials. In line with previous studies, Deg materials showed a higher YAP nuclear translocation
564 compared to noDeg, triggered solely by the degradation of the material [31][30][62]. Our research
565 takes this effect further by evaluating the enhanced mechanotransduction effect in patterned materials
566 compared to single-phase counterparts (Fig 7A-I). The enhanced hMSCs spreading and collective

567 cell alignment resulting from the anisotropic material interphases, seem to enhance
568 mechanosensation by YAP nuclear translocation. As underlying mechanism, we identify two key
569 factors: matrix degradation (as no YAP nuclear translocation was observed in MMPscr materials,
570 Fig. 7J-N) and the need of cell-matrix adhesion via integrin activation (as no YAP nuclear
571 translocation was observed in noRGD materials, Fig. 7O-S). This ultimately leads to enhanced
572 mechanotransduction and osteogenic differentiation in anisotropic hydrogels.

573 The research presented in this paper represents a contribution to the basic understanding of how cells
574 interact with multicompartment materials. In the future, further research will be required to
575 understand the *in vivo* implications of anisotropic materials.

576 **5 Conclusions**

577 In summary, we show that anisotropic hydrogel degradation enhances hMSC cell spreading in 3D,
578 collective cell alignment, mechanotransduction and osteogenic differentiation, compared to the
579 single-phase equivalents. Patterned material´s interphase proximity, matrix-bound cell adhesion
580 peptide RGD and degradable crosslinking peptides are required for patterned mechanosensing. These
581 combined results highlight the importance of developing 3D patterned biomaterials to mimic the
582 anisotropy in biological tissues, for both fundamental understanding of guided collective cell
583 behavior and tissue anisotropy, as well as for applications in biofabrication and tissue engineering.

584 **6 Acknowledgements**

585 The authors acknowledge the support from all group members of Cipitria, Schmidt-Bleek and Duda's
586 laboratories. We thank the Cell Core Facility of Charité-Universitätsmedizin for providing the cells
587 used in this study. In addition, we thank the Research Workshop at the Charité-Universitätsmedizin
588 Berlin for developing and manufacturing some experimental devices. We thank Andreas Engels for

printing the photomasks used in this research. We thank Mario Thiele from Charité-Universitätsmedizin and Samik Real from Hasso Plattner-Institute for contributing with the macros used in this research. In addition to the support given by Ansgar Petersen and Erik Brauer from JWI.

7 CRediT authorship contribution statement

A Cipitria conceived the idea. CA Garrido, A Cipitria developed the methodology. CA Garrido, DS Garske performed the experiments. CH Bucher performed the flow cytometry experiments and data analysis. S Amini supported the micro indentation experiments. CA Garrido quantified and analyzed the data. CA Garrido and A Cipitria drafted the manuscript. DS Garske contributed with the visualization of the data. A Cipitria, K Schmidt-Bleek and GN Duda supervised, reviewed and edited the original data and manuscript. All authors discussed the results and contributed to the final manuscript.

8 Declaration of competing interest

The authors declare that the research was conducted in the absence of any commercial or financial relationships that could be considered as a potential conflict of interest.

9 Funding

This work was funded by the Deutsche Forschungsgemeinschaft (DFG) Collaborative Research Center (CRC) 1444 grant (C.A.G, D.S.G.). A. Cipitria is grateful for financial support from the DFG Emmy Noether grant (CI 203/2-1), IKERBASQUE Basque Foundation for Science, the Spanish Ministry of Science and Innovation (PID2021-123013OB-I00 funded by MCIN/AEI/10.13039/501100011033/FEDER, UE), and the European Research Council Consolidator Grant (DORMATRIX, 101123883). Funded by the European Union. Views and opinions expressed are however those of the author(s) only and do not necessarily reflect those of the European Union or

the European Research Council Executive Agency. Neither the European Union nor the granting authority can be held responsible for them.

10 Data and code availability

All raw and processed data are available in the publicly accessible Edmond repository of the Max Planck Society: https://doi.org/10.17617/3.WLTITB

11 References

[1] M. Krampera, K. Le Blanc, Mesenchymal stromal cells: Putative microenvironmental modulators become cell therapy, Cell Stem Cell 28 (2021) 1708–1725. https://doi.org/10.1016/j.stem.2021.09.006.

[2] A.C. Wilkinson, K.J. Igarashi, H. Nakauchi, Haematopoietic stem cell self-renewal in vivo and ex vivo, Nat. Rev. Genet. 21 (2020) 541–554. https://doi.org/10.1038/s41576-020-0241-0.

[3] H.S. Kim, S.G. Kumbar, S.P. Nukavarapu, Biomaterial-directed cell behavior for tissue engineering, Curr. Opin. Biomed. Eng. 17 (2021) 100260. https://doi.org/10.1016/j.cobme.2020.100260.

[4] C.A. Deforest, K.S. Anseth, Advances in bioactive hydrogels to probe and direct cell fate, Annu. Rev. Chem. Biomol. Eng. 3 (2012) 421–444. https://doi.org/10.1146/annurev-chembioeng-062011-080945.

[5] E.C. González-Díaz, S. Varghese, Hydrogels as extracellular matrix analogs, Gels 2 (2016). https://doi.org/10.3390/gels2030020.

[6] A.M. Kloxin, C.J. Kloxin, C.N. Bowman, K.S. Anseth, Mechanical properties of cellularly responsive hydrogels and their experimental determination, Adv. Mater. 22 (2010) 3484–3494. https://doi.org/10.1002/adma.200904179.

[7] M. Guvendiren, J.A. Burdick, Engineering synthetic hydrogel microenvironments to instruct stem cells, Curr. Opin. Biotechnol. 24 (2013) 841–846. https://doi.org/10.1016/j.copbio.2013.03.009.

[8] L.R. Smith, S. Cho, D.E. Discher, Stem cell differentiation is regulated by extracellular matrix mechanics, Physiology 33 (2018) 16–25. https://doi.org/10.1152/physiol.00026.2017.

[9] C. Branco da Cunha, D.D. Klumpers, W.A. Li, S.T. Koshy, J.C. Weaver, O. Chaudhuri, P.L. Granja, D.J. Mooney, Influence of the stiffness of three-dimensional alginate/collagen-I interpenetrating networks on fibroblast biology, Biomaterials 35 (2014) 8927–8936. https://doi.org/10.1016/j.biomaterials.2014.06.047.

[10] N. Huebsch, E. Lippens, K. Lee, M. Mehta, S.T. Koshy, M.C. Darnell, R.M. Desai, C.M. Madl, M. Xu, X. Zhao, O. Chaudhuri, C. Verbeke, W.S. Kim, K. Alim, A. Mammoto, D.E. Ingber, G.N. Duda, D.J. Mooney, Matrix elasticity of void-forming hydrogels controls transplanted-stem-cell-mediated bone formation, Nat. Mater. 14 (2015) 1269–1277. https://doi.org/10.1038/nmat4407.

[11] O. Chaudhuri, L. Gu, D. Klumpers, M. Darnell, S.A. Bencherif, J.C. Weaver, N. Huebsch, H. Lee, E. Lippens, G.N. Duda, D.J. Mooney, Hydrogels with tunable stress relaxation regulate stem cell fate and activity, Nat. Mater. 15 (2016) 326–334. https://doi.org/10.1038/nmat4489.

[12] O. Chaudhuri, J. Cooper-White, P.A. Janmey, D.J. Mooney, V.B. Shenoy, Effects of extracellular matrix viscoelasticity on cellular behaviour, Nature 584 (2020) 535–546. https://doi.org/10.1038/s41586-020-2612-2.

[13] S. Khetan, M. Guvendiren, W.R. Legant, D.M. Cohen, C.S. Chen, J.A. Burdick, Degradation-mediated cellular traction directs stem cell fate in covalently crosslinked three-dimensional hydrogels, Nat. Mater. 12 (2013) 458–465. https://doi.org/10.1038/nmat3586.

[14] V. V. Rao, M.E. Wechsler, E. Cravens, S.J. Wojda, A.S. Caldwell, B.E. Kirkpatrick, S.W. Donahue, K.S. Anseth, Granular PEG hydrogels mediate osteoporotic MSC clustering via N-cadherin influencing the pro-resorptive bias of their secretory profile, Acta Biomater. 145 (2022) 77–87. https://doi.org/10.1016/j.actbio.2022.04.023.

[15] M.D. Davidson, E. Ban, A.C.M. Schoonen, M.H. Lee, M. D'Este, V.B. Shenoy, J.A. Burdick, Mechanochemical Adhesion and Plasticity in Multifiber Hydrogel Networks, Adv. Mater. 32 (2020) 1–8. https://doi.org/10.1002/adma.201905719.

[16] A. Sanchez-Rubio, V. Jayawarna, E. Maxwell, M.J. Dalby, M. Salmeron-Sanchez, Keeping It Organized: Multicompartment Constructs to Mimic Tissue Heterogeneity, Adv. Healthc. Mater. (2023) 2202110. https://doi.org/10.1002/adhm.202202110.

[17] N. Broguiere, I. Lüchtefeld, L. Trachsel, D. Mazunin, R. Rizzo, J.W. Bode, M.P. Lutolf, M. Zenobi-Wong, Morphogenesis Guided by 3D Patterning of Growth Factors in Biological Matrices, Adv. Mater. 32 (2020) 1–10. https://doi.org/10.1002/adma.201908299.

[18] C.A. DeForest, K.S. Anseth, Cytocompatible click-based hydrogels with dynamically tunable properties through orthogonal photoconjugation and photocleavage reactions, Nat. Chem. 3 (2011) 925–931. https://doi.org/10.1038/nchem.1174.

[19] K.H. Song, C.B. Highley, A. Rouff, J.A. Burdick, Complex 3D-Printed Microchannels within Cell-Degradable Hydrogels, Adv. Funct. Mater. 28 (2018) 1–10. https://doi.org/10.1002/adfm.201801331.

[20] A. Thomas, I. Orellano, T. Lam, B. Noichl, M.A. Geiger, A.K. Amler, A.E. Kreuder, C. Palmer, G. Duda, R. Lauster, L. Kloke, Vascular bioprinting with enzymatically degradable bioinks via multi-material projection-based stereolithography, Acta Biomater. 117 (2020) 121–132. https://doi.org/10.1016/J.ACTBIO.2020.09.033.

[21] D. Hanjaya-Putra, K.T. Wong, K. Hirotsu, S. Khetan, J.A. Burdick, S. Gerecht, Spatial control of cell-mediated degradation to regulate vasculogenesis and angiogenesis in hyaluronan hydrogels, Biomaterials 33 (2012) 6123–6131. https://doi.org/10.1016/j.biomaterials.2012.05.027.

[22] B. Trappmann, B.M. Baker, W.J. Polacheck, C.K. Choi, J.A. Burdick, C.S. Chen, Matrix degradability controls multicellularity of 3D cell migration, Nat. Commun. 8 (2017) 371. https://doi.org/10.1038/s41467-017-00418-6.

[23] C.A. Garrido, D.S. Garske, M. Thiele, S. Amini, S. Real, G.N. Duda, K. Schmidt-Bleek, A. Cipitria, Hydrogels with stiffness-degradation spatial patterns control anisotropic 3D cell response, Biomater. Adv. 151 (2023) 2023.01.25.525504. https://doi.org/10.1016/j.bioadv.2023.213423.

[24] S. Khetan, J.A. Burdick, Patterning network structure to spatially control cellular remodeling and stem cell fate within 3-dimensional hydrogels, Biomaterials 31 (2010) 8228–8234. https://doi.org/10.1016/j.biomaterials.2010.07.035.

[25] L.G. Vincent, A.J. Engler, Stem cell differentiation: Post-degradation forces kick in, Nat. Mater. 12

686 (2013) 384–386. https://doi.org/10.1038/nmat3636.

687 [26] A. Lueckgen, D.S. Garske, A. Ellinghaus, D.J. Mooney, G.N. Duda, A. Cipitria, Enzymatically-
688 degradable alginate hydrogels promote cell spreading and in vivo tissue infiltration, Biomaterials 217
689 (2019) 119294. https://doi.org/10.1016/j.biomaterials.2019.119294.

690 [27] S. Khetan, M. Guvendiren, W.R. Legant, D.M. Cohen, C.S. Chen, J.A. Burdick, Degradation-mediated
691 cellular traction directs stem cell fate in covalently crosslinked three-dimensional hydrogels, Nat.
692 Mater. 12 (2013) 458–465. https://doi.org/10.1038/nmat3586.

693 [28] S. Dupont, L. Morsut, M. Aragona, E. Enzo, S. Giulitti, M. Cordenonsi, F. Zanconato, J. Le Digabel,
694 M. Forcato, S. Bicciato, N. Elvassore, S. Piccolo, Role of YAP/TAZ in mechanotransduction, Nature
695 474 (2011) 179–183. https://doi.org/10.1038/nature10137.

696 [29] A. Saraswathibhatla, D. Indana, O. Chaudhuri, Cell–extracellular matrix mechanotransduction in 3D,
697 Nat. Rev. Mol. Cell Biol. (2023) 1–22. https://doi.org/10.1038/s41580-023-00583-1.

698 [30] S.R. Caliari, S.L. Vega, M. Kwon, E.M. Soulas, J.A. Burdick, Dimensionality and spreading influence
699 MSC YAP/TAZ signaling in hydrogel environments, Biomaterials 103 (2016) 314–323.
700 https://doi.org/10.1016/j.biomaterials.2016.06.061.

701 [31] N. Gjorevski, N. Sachs, A. Manfrin, S. Giger, M.E. Bragina, P. Ordóñez-Morán, H. Clevers, M.P.
702 Lutolf, Designer matrices for intestinal stem cell and organoid culture, Nature 539 (2016) 560–564.
703 https://doi.org/10.1038/nature20168.

704 [32] X. Cai, K.C. Wang, Z. Meng, Mechanoregulation of YAP and TAZ in Cellular Homeostasis and
705 Disease Progression, Front. Cell Dev. Biol. 9 (2021) 1–12. https://doi.org/10.3389/fcell.2021.673599.

706 [33] N. Gjorevski, M. Nikolaev, T.E. Brown, O. Mitrofanova, N. Brandenberg, F.W. DelRio, F.M. Yavitt,
707 P. Liberali, K.S. Anseth, M.P. Lutolf, Tissue geometry drives deterministic organoid patterning,
708 Science (80-.). 375 (2022). https://doi.org/10.1126/science.aaw9021.

709 [34] S. Reinke, S. Geissler, W.R. Taylor, K. Schmidt-Bleek, K. Juelke, V. Schwachmeyer, M. Dahne, T.
710 Hartwig, L. Akyüz, C. Meisel, N. Unterwalder, N.B. Singh, P. Reinke, N.P. Haas, H.-D. Volk, G.N.
711 Duda, Terminally Differentiated CD8 + T Cells Negatively Affect Bone Regeneration in Humans, Sci.
712 Transl. Med. 5 (2013) 177ra36-177ra36. https://doi.org/10.1126/scitranslmed.3004754.

713 [35] A. Andrzejewska, R. Catar, J. Schoon, T.H. Qazi, F.A. Sass, D. Jacobi, A. Blankenstein, S. Reinke, D.
714 Krüger, M. Streitz, S. Schlickeiser, S. Richter, N. Souidi, C. Beez, J. Kamhieh-Milz, U. Krüger, T.
715 Zemojtel, K. Jürchott, D. Strunk, P. Reinke, G. Duda, G. Moll, S. Geissler, Multi-Parameter Analysis
716 of Biobanked Human Bone Marrow Stromal Cells Shows Little Influence for Donor Age and Mild
717 Comorbidities on Phenotypic and Functional Properties, Front. Immunol. 10 (2019) 1–24.
718 https://doi.org/10.3389/fimmu.2019.02474.

719 [36] M.L. Oyen, Mechanical characterisation of hydrogel materials, Int. Mater. Rev. 59 (2014) 44–59.
720 https://doi.org/10.1179/1743280413Y.0000000022.

721 [37] K.S. Anseth, C.N. Bowman, L. Brannon-Peppas, Mechanical properties of hydrogels and their
722 experimental determination, Biomaterials 17 (1996) 1647–1657. https://doi.org/10.1016/0142-
723 9612(96)87644-7.

724 [38] S.T. Koshy, R.M. Desai, P. Joly, J. Li, R.K. Bagrodia, S.A. Lewin, N.S. Joshi, D.J. Mooney, Click-
725 Crosslinked Injectable Gelatin Hydrogels, Adv. Healthc. Mater. 5 (2016) 541–547.
726 https://doi.org/10.1002/adhm.201500757.

[39] C.A. Schneider, W.S. Rasband, K.W. Eliceiri, NIH Image to ImageJ: 25 years of image analysis, Nat. Methods 9 (2012) 671–675. https://doi.org/10.1038/nmeth.2089.

[40] Z.Q. Liu, Scale space approach to directional analysis of images., Appl. Opt. 30 (1991) 1369–1373. https://doi.org/10.1364/AO.30.001369.

[41] J.B. Kelley, B.M. Paschal, Fluorescence-based quantification of nucleocytoplasmic transport, Methods 157 (2019) 106–114. https://doi.org/10.1016/j.ymeth.2018.11.002.

[42] C.H. Bucher, J.C. Berkmann, L.M. Burkhardt, C. Paschke, C. Schlundt, A. Lang, A. Wolter, A. Damerau, S. Geissler, H.D. Volk, G.N. Duda, K. Schmidt-Bleek, Local immune cell contributions to fracture healing in aged individuals – A novel role for interleukin 22, Exp. Mol. Med. 54 (2022) 1262–1276. https://doi.org/10.1038/s12276-022-00834-9.

[43] T.M. Ashhurst, F. Marsh-Wakefield, G.H. Putri, A.G. Spiteri, D. Shinko, M.N. Read, A.L. Smith, N.J.C. King, Integration, exploration, and analysis of high-dimensional single-cell cytometry data using Spectre, Cytom. Part A 101 (2022) 237–253. https://doi.org/10.1002/cyto.a.24350.

[44] M. Bao, J. Xie, N. Katoele, X. Hu, B. Wang, A. Piruska, W.T.S. Huck, Cellular Volume and Matrix Stiffness Direct Stem Cell Behavior in a 3D Microniche, ACS Appl. Mater. Interfaces 11 (2019) 1754–1759. https://doi.org/10.1021/acsami.8b19396.

[45] G. Devi, A.K. Hedger, R.J. Whitby, J.K. Watts, Double Click: Unexpected 1:2 Stoichiometry in a Norbornene–Tetrazine Reaction, J. Org. Chem. 88 (2023) 5341–5347. https://doi.org/10.1021/acs.joc.2c02861.

[46] S.B. Anderson, C.C. Lin, D. V. Kuntzler, K.S. Anseth, The performance of human mesenchymal stem cells encapsulated in cell-degradable polymer-peptide hydrogels, Biomaterials 32 (2011) 3564–3574. https://doi.org/10.1016/j.biomaterials.2011.01.064.

[47] D.M. Le, K. Kulangara, A.F. Adler, K.W. Leong, V.S. Ashby, Dynamic topographical control of mesenchymal stem cells by culture on responsive poly(Ïµ-caprolactone) surfaces, Adv. Mater. 23 (2011) 3278–3283. https://doi.org/10.1002/adma.201100821.

[48] S. Li, Y. Sun, Y. Chen, J. Lu, G. Jiang, K. Yu, Y. Wu, Y. Mao, H. Jin, J. Luo, S. Dong, B. Hu, Y. Ding, A. Liu, Y. Shen, G. Feng, S. Yan, Y. He, R. Yan, Sandwich Biomimetic Scaffold Based Tendon Stem/Progenitor Cell Alignment in a 3D Microenvironment for Functional Tendon Regeneration, ACS Appl. Mater. Interfaces 15 (2023) 4652–4667. https://doi.org/10.1021/acsami.2c16584.

[49] M. Ventre, F. Causa, P.A. Netti, Determinants of cell-material crosstalk at the interface: Towards engineering of cell instructive materials, J. R. Soc. Interface 9 (2012) 2017–2032. https://doi.org/10.1098/rsif.2012.0308.

[50] K.O. Okeyo, Y. Kibe, T. Adachi, Controlling macroscale cell alignment in self-organized cell sheets by tuning the microstructure of adhesion-limiting micromesh scaffolds, Mater. Today Adv. 12 (2021) 100194. https://doi.org/10.1016/j.mtadv.2021.100194.

[51] M. Werner, N.A. Kurniawan, G. Korus, C.V.C. Bouten, A. Petersen, Mesoscale substrate curvature overrules nanoscale contact guidance to direct bone marrow stromal cell migration, J. R. Soc. Interface 15 (2018). https://doi.org/10.1098/rsif.2018.0162.

[52] J. Knychala, N. Bouropoulos, C.J. Catt, O.L. Katsamenis, C.P. Please, B.G. Sengers, Pore geometry regulates early stage human bone marrow cell tissue formation and organisation, Ann. Biomed. Eng. 41 (2013) 917–930. https://doi.org/10.1007/s10439-013-0748-z.

[53] Y. Li, G. Huang, X. Zhang, L. Wang, Y. Du, T.J. Lu, F. Xu, Engineering cell alignment in vitro, Biotechnol. Adv. 32 (2014) 347–365. https://doi.org/10.1016/j.biotechadv.2013.11.007.

[54] M. Murshed, Mechanism of bone mineralization, Cold Spring Harb. Perspect. Med. 8 (2018) 1–11. https://doi.org/10.1101/CSHPERSPECT.A031229.

[55] M.S. Choudhery, R. Mahmood, D.T. Harris, F.J. Ahmad, Minimum criteria for defining induced mesenchymal stem cells, Cell Biol. Int. 46 (2022) 986–989. https://doi.org/10.1002/cbin.11790.

[56] H. Busser, M. Najar, G. Raicevic, K. Pieters, R. Velez Pombo, P. Philippart, N. Meuleman, D. Bron, L. Lagneaux, Isolation and Characterization of Human Mesenchymal Stromal Cell Subpopulations: Comparison of Bone Marrow and Adipose Tissue, Stem Cells Dev. 24 (2015) 2142–2157. https://doi.org/10.1089/scd.2015.0172.

[57] A. Valdivia, A.M. Avalos, L. Leyton, Thy-1 (CD90)-regulated cell adhesion and migration of mesenchymal cells: insights into adhesomes, mechanical forces, and signaling pathways, Front. Cell Dev. Biol. 11 (2023) 1–23. https://doi.org/10.3389/fcell.2023.1221306.

[58] L. Leyton, J. Díaz, S. Martínez, E. Palacios, L.A. Pérez, R.D. Pérez, Thy-1/CD90 a Bidirectional and Lateral Signaling Scaffold, Front. Cell Dev. Biol. 7 (2019) 1–11. https://doi.org/10.3389/fcell.2019.00132.

[59] A. Ode, J. Kopf, K. Schmidt-Bleek, P. Schrade, P. Kolar, F. Buttgereit, K. Lehmann, D. Hutmacher, G. Duda, G. Kasper, CD73 and CD29 concurrently mediate the mechanically induced decrease of migratory capacity of mesenchymal stromal cells, Eur. Cells Mater. 45 (2011) 26–42.

[60] S.A. Lund, C.M. Giachelli, M. Scatena, The role of osteopontin in inflammatory processes, J. Cell Commun. Signal. 3 (2009) 311–322. https://doi.org/10.1007/s12079-009-0068-0.

[61] S. Bakhshandeh, U. Heras, H.M. Taïeb, A.R. Varadarajan, S.M. Lissek, S.M. Hücker, X. Lu, D.S. Garske, S.A.E. Young, A. Abaurrea, M.M. Caffarel, A. Riestra, P. Bragado, J. Contzen, M. Gossen, S. Kirsch, J. Warfsmann, K. Honarnejad, C.A. Klein, A. Cipitria, Dormancy-inducing 3D engineered matrix uncovers mechanosensitive and drug-protective FHL2-p21 signaling axis, Sci. Adv. 10 (2024). https://doi.org/10.1126/sciadv.adr3997.

[62] S.R. Caliari, S.L. Vega, M. Kwon, E.M. Soulas, J.A. Burdick, Dimensionality and spreading influence MSC YAP/TAZ signaling in hydrogel environments, Biomaterials 103 (2016) 314–323. https://doi.org/10.1016/j.biomaterials.2016.06.061.

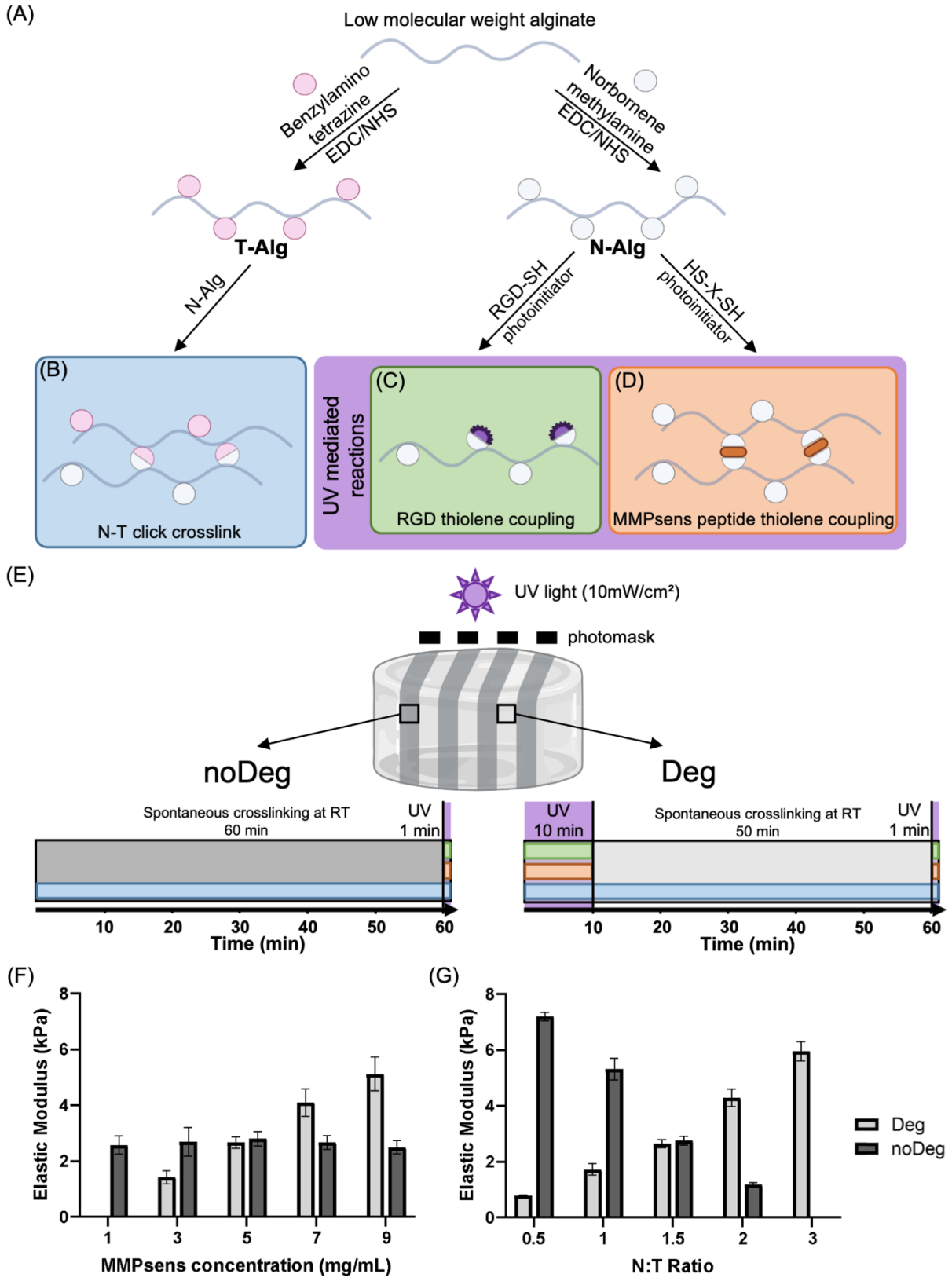

Figure 1: Description of the material chemistry. Scheme of the carbodiimide coupling of norbornene or tetrazine groups to the alginate backbone (A). Scheme of non-degradable bonds

through Diels-Alder spontaneous click crosslinking of norbornene and tetrazine (B, blue). UV light dependent thiol-ene reactions of norbornene groups with RGD (C, green) and MMPsens peptide crosslinker (X: GCRD-VPMS ↓ MRGG-DRCG) (D, orange). Time scheme depicting the different reactions occurring during the dual crosslinking (E). Material elastic modulus can be tuned through the MMPsens concentration, for a constant N:T ratio of 1.5 (F) and also through varying the N:T ratio, for a constant MMPsens concentration of 5 mg/mL (G).

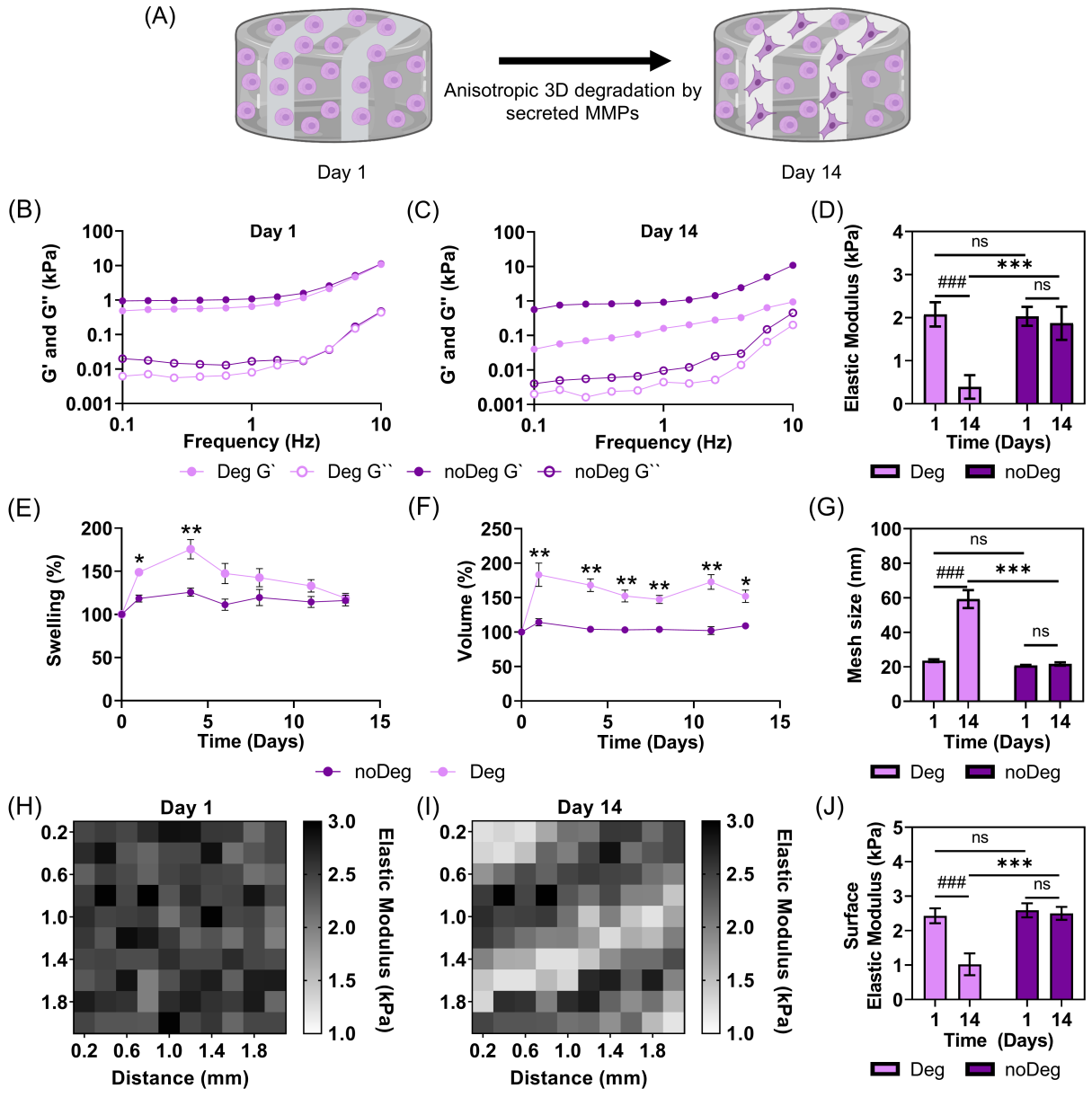

809 **Figure 2: Changes in mechanical properties and swelling over time of cell-laden anisotropic**
810 **hydrogels.** Anisotropic dual crosslinking results in 3D patterns of hydrogel degradation due to cell-
811 derived enzymatic action (A). Representative plots of G′ (storage modulus, ●) and G′′ (loss modulus,
812 ○) obtained by rheology of noDeg single-phase (dark purple) and Deg single-phase (light purple)
813 materials, on day 1 (B) and day 14 (C) from n = 6 gels. Elastic modulus (D) and corresponding mesh
814 size (G), approximated from rheology data. Swelling (E) and volume (F) changes over time (relative
815 to 2h after equilibration), from n = 3 gels. Representative microindentation map of the surface elastic
816 modulus on day 1 (H) and day 14 (I), 10x10 grid, indentation spacing of 200 µm. Surface elastic
817 modulus in Deg and noDeg phases obtained by microindentation, averaging all indents in a specific
818 region of patterned materials on day 1 and day 14 (J). Statistical significance with ANOVA and
819 Bonferroni correction.

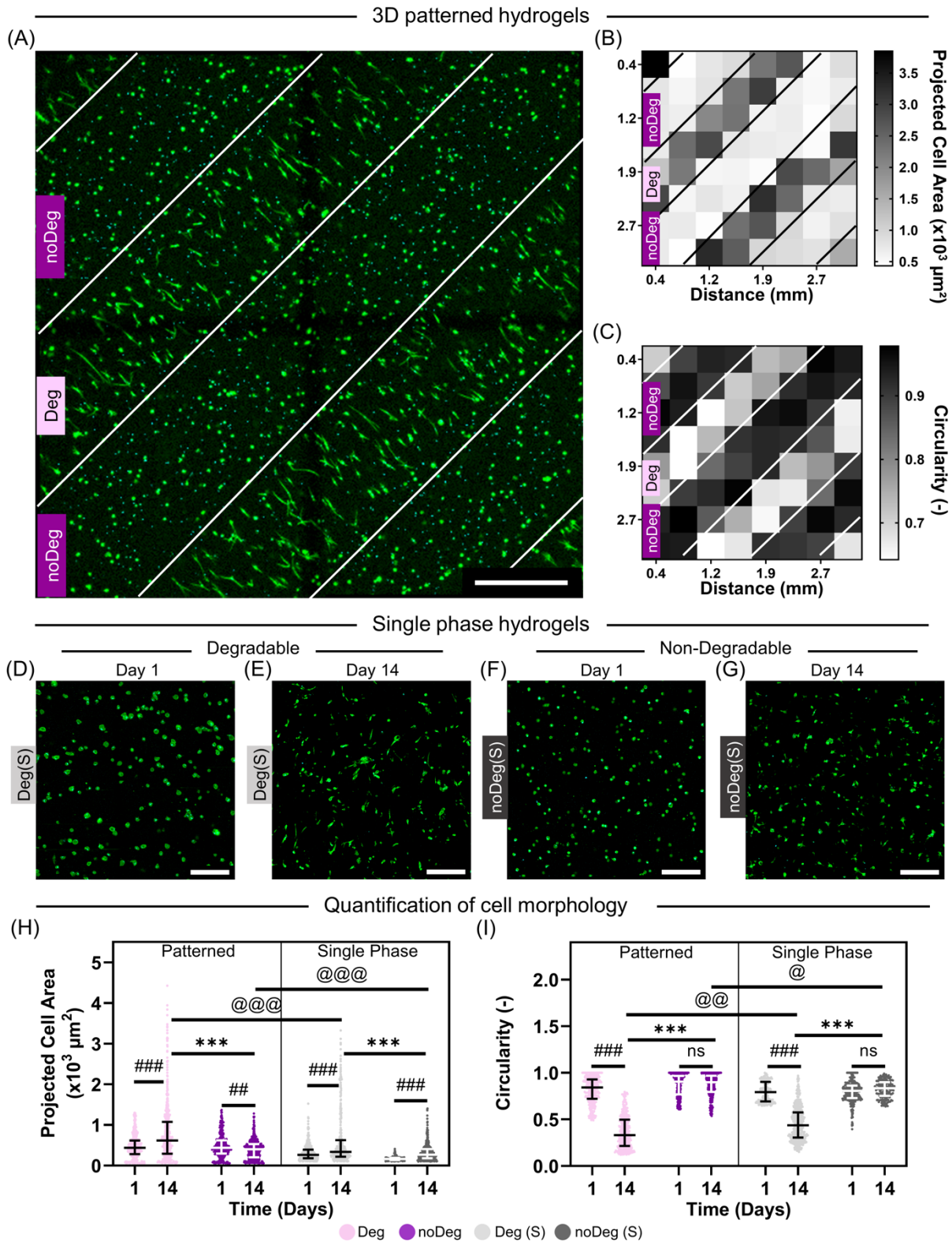

820

821 **Figure 3: Anisotropic hMSC morphology in patterned materials on day 14.** Representative

822 confocal images of actin (Phalloidin/green) and nucleus (SYTOX/cyan) staining of patterned

823 materials with hMSCs in growth media (A). Heatmap quantification with an 8x8 grid of projected
824 cell area (B) and cell circularity (C). Single-phase materials representative confocal images of actin
825 (Phalloidin/green) and nucleus (SYTOX/cyan) staining on day 1 (Deg (D) and noDeg (F)) and day
826 14 (Deg (E) and noDeg (G)). Dot graph of raw data (> 400 single cells per phase and condition) of
827 projected cell area (H) and circularity (I) on day 14 (see Suppl. Fig. S4A-C for corresponding images
828 and heat maps on day 1). Statistical significance with Kruskal-Wallis and Dunn's correction). Scale
829 bar: 500 µm (A) and 250 µm (D-G).

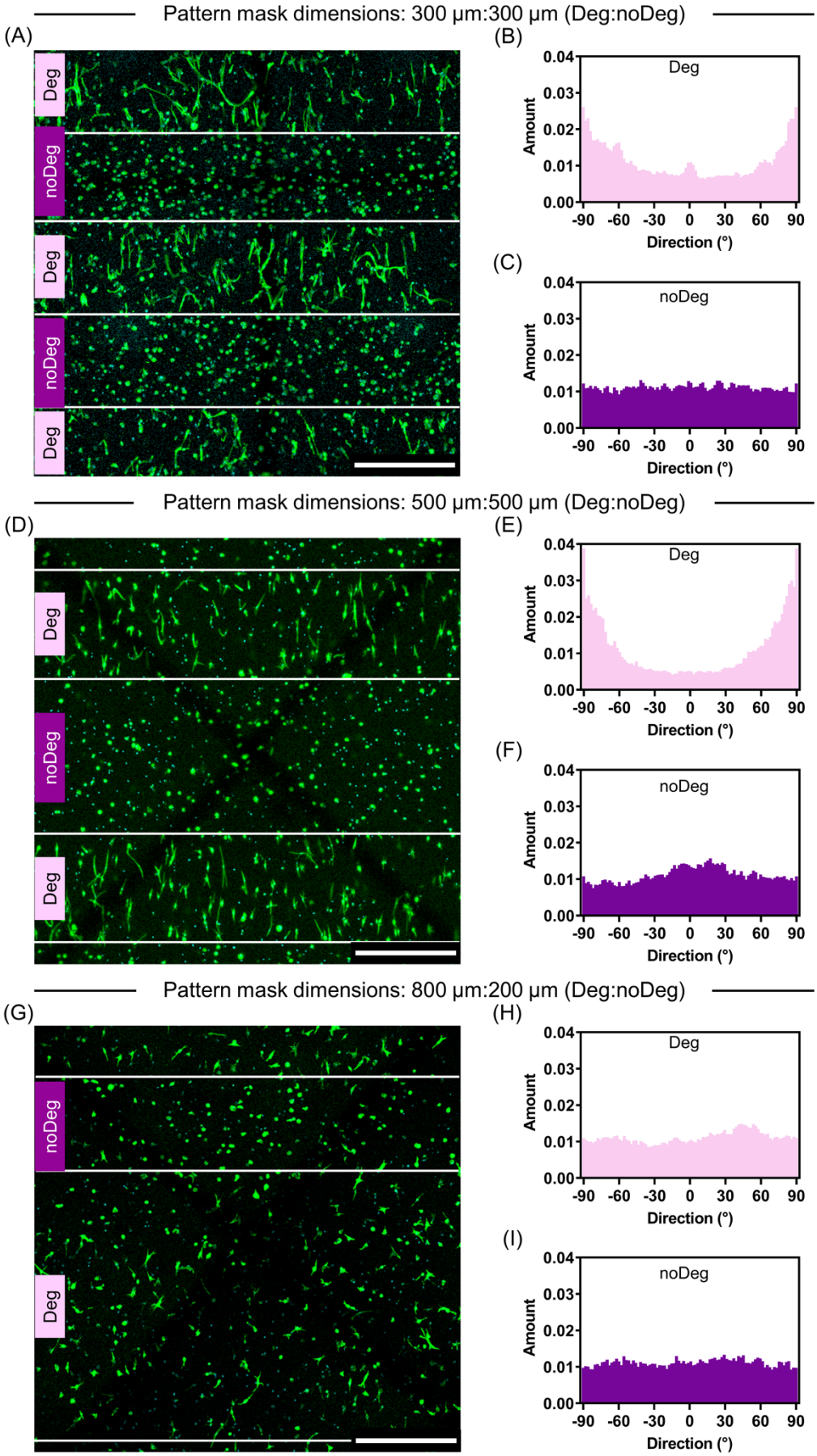
Pattern mask dimensions: 300 µm:300 µm (Deg:noDeg)
(A)
Deg
noDeg
Deg
noDeg
Deg
(B)
Deg
Amount
0.04
0.03
0.02
0.01
0.00
-90 -60 -30 0 30 60 90
Direction (°)
(C)
noDeg
Amount
0.04
0.03
0.02
0.01
0.00
-90 -60 -30 0 30 60 90
Direction (°)
Pattern mask dimensions: 500 µm:500 µm (Deg:noDeg)
(D)
Deg
noDeg
Deg
(E)
Deg
Amount
0.04
0.03
0.02
0.01
0.00
-90 -60 -30 0 30 60 90
Direction (°)
(F)
noDeg
Amount
0.04
0.03
0.02
0.01
0.00
-90 -60 -30 0 30 60 90
Direction (°)
Pattern mask dimensions: 800 µm:200 µm (Deg:noDeg)
(G)
noDeg
Deg
(H)
Deg
Amount
0.04
0.03
0.02
0.01
0.00
-90 -60 -30 0 30 60 90
Direction (°)
(I)
noDeg
Amount
0.04
0.03
0.02
0.01
0.00
-90 -60 -30 0 30 60 90
Direction (°)

830

831 **Figure 4: Collective cell alignment of encapsulated hMSCs in patterned materials with different**
832 **photomask dimensions on day 14.** Patterned materials fabricated with photomasks of different
833 Deg:noDeg dimensions: 300 µm:300 µm (A-C), 500 µm:500 µm (D-F) and 800 µm:200 µm (G-I).
834 Representative confocal images of actin (Phalloidin/green) and nucleus (SYTOX, cyan) staining of
835 patterned materials with hMSCs (A, D, G) and histograms indicating the distribution of the collective
836 cell alignment angle in Deg and noDeg phases of patterned materials (B/C, E/F, H/I), with $n > 200$
837 cells per phase. Scale bar: 500 µm.

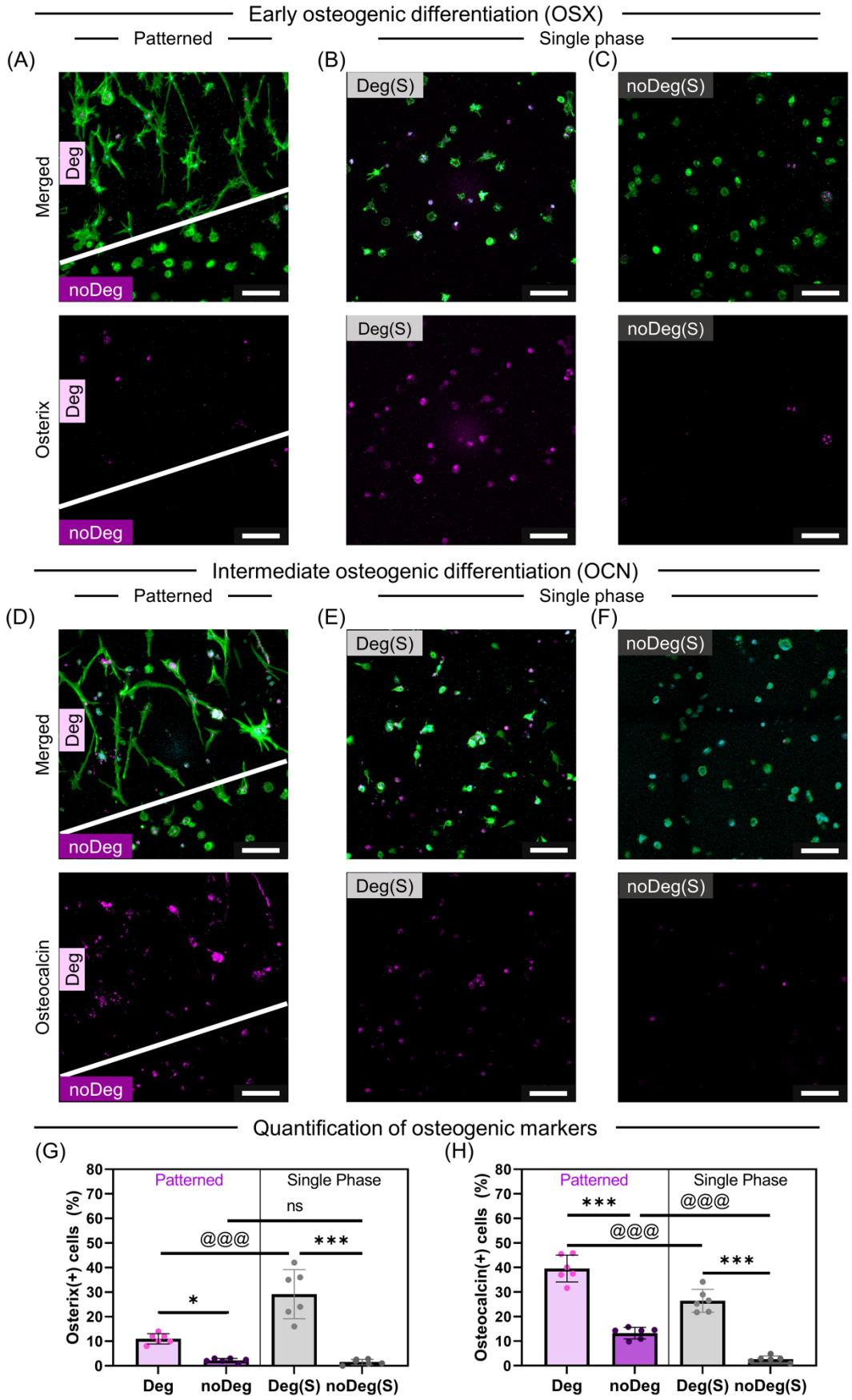
Early osteogenic differentiation (OSX)
Patterned
Single phase
(A)
(B)
(C)
Merged
Osterix
Deg
noDeg
Deg(S)
noDeg(S)
Intermediate osteogenic differentiation (OCN)
(D)
(E)
(F)
Osteocalcin
Quantification of osteogenic markers
(G)
(H)
Osterix(+) cells (%)
Osteocalcin(+) cells (%)
Patterned
Single Phase
ns
@@@
***
*
Deg
noDeg
Deg(S)
noDeg(S)

838

839 **Figure 5: Osteogenic differentiation of encapsulated hMSCs in patterned materials on day 14.**
840 Actin (Phalloidin/green) and nucleus (SYTOX/cyan) staining with Osterix (OSX, magenta, A-C) or
841 Osteocalcin (OCN, magenta, D-F). Comparison between patterned materials (A, D), single-phase
842 Deg(S) (B, E) and single-phase noDeg(S) (C, F), quantified in bar plots (G, H), which show the mean
843 and standard deviation of n = 6 fields of view containing multiple cells (n ≥ 150 cells per phase and
844 condition). Statistical significance with ANOVA and Bonferroni correction. Scale bar: 100 µm.

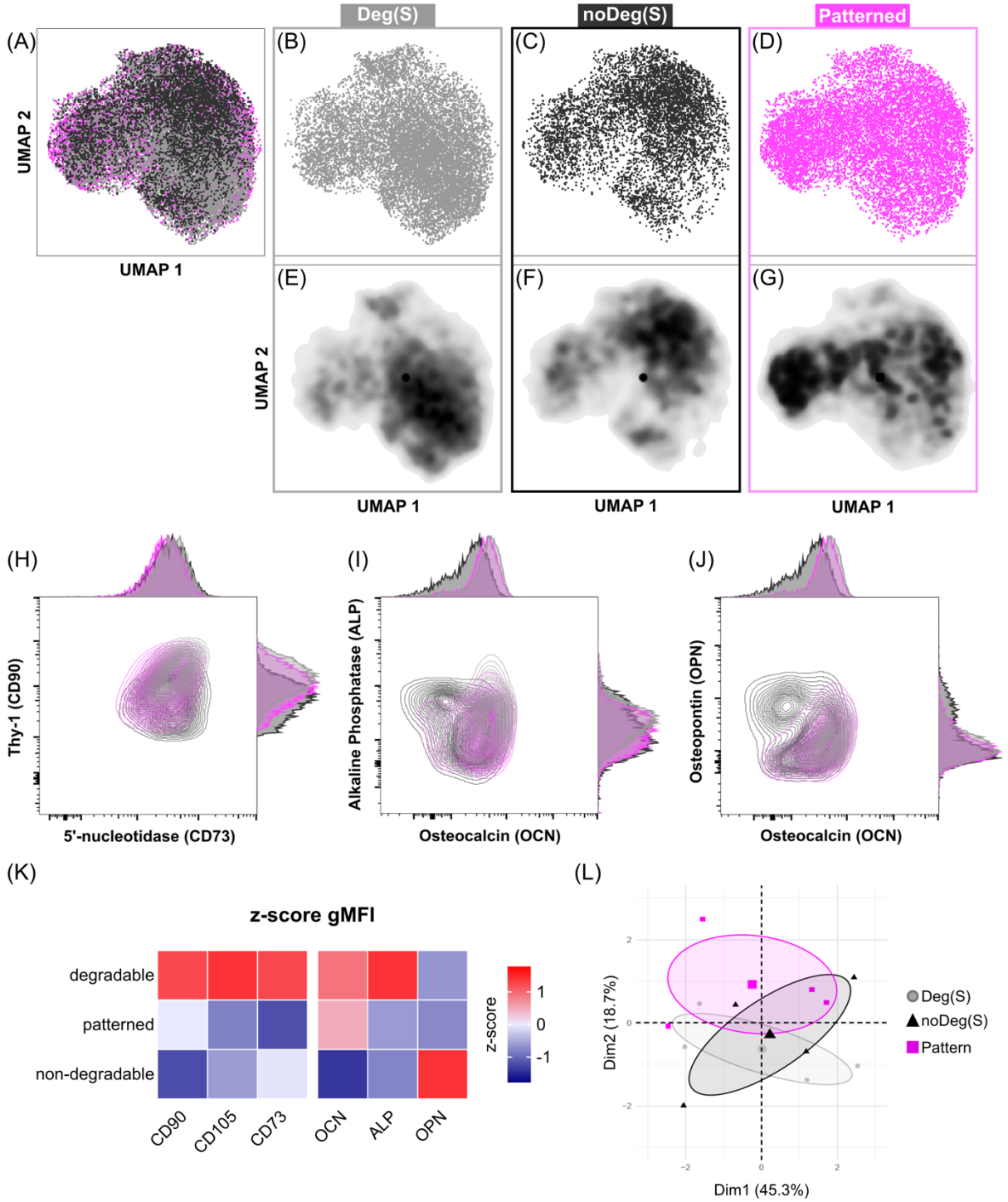

845

846 **Figure 6: Flow cytometry evaluation of hMSCs retrieved from 3D patterned and single-phase**

847 **materials after culturing for 14 days.** UMAPs cluster plots merged (A), Deg(S) (B), noDeg(S) (C)

848 and patterned (D), and the corresponding density plots of Deg(S) (E), noDeg(S) (F) and patterned

849 (G). Multiplots, contour plots plus histograms of the expression of: CD73 vs. CD90 (H), OCN vs.

850 ALP (I) and OCN vs. OPN (J). z-score quantification of hMSCs minimal criteria markers (CD105,
851 CD73, CD90) and differentiation markers (OCN, ALP, OPN) (K). Principal component analysis for
852 dimension 1 (Dim 1, 45,3 %) and dimension 2 (Dim 2, 18,7 %), the big symbols show the center of
853 the ellipse and the smaller symbols the different batches (L). n = 4 batches containing $1x10^5$ cells, for
854 each material.

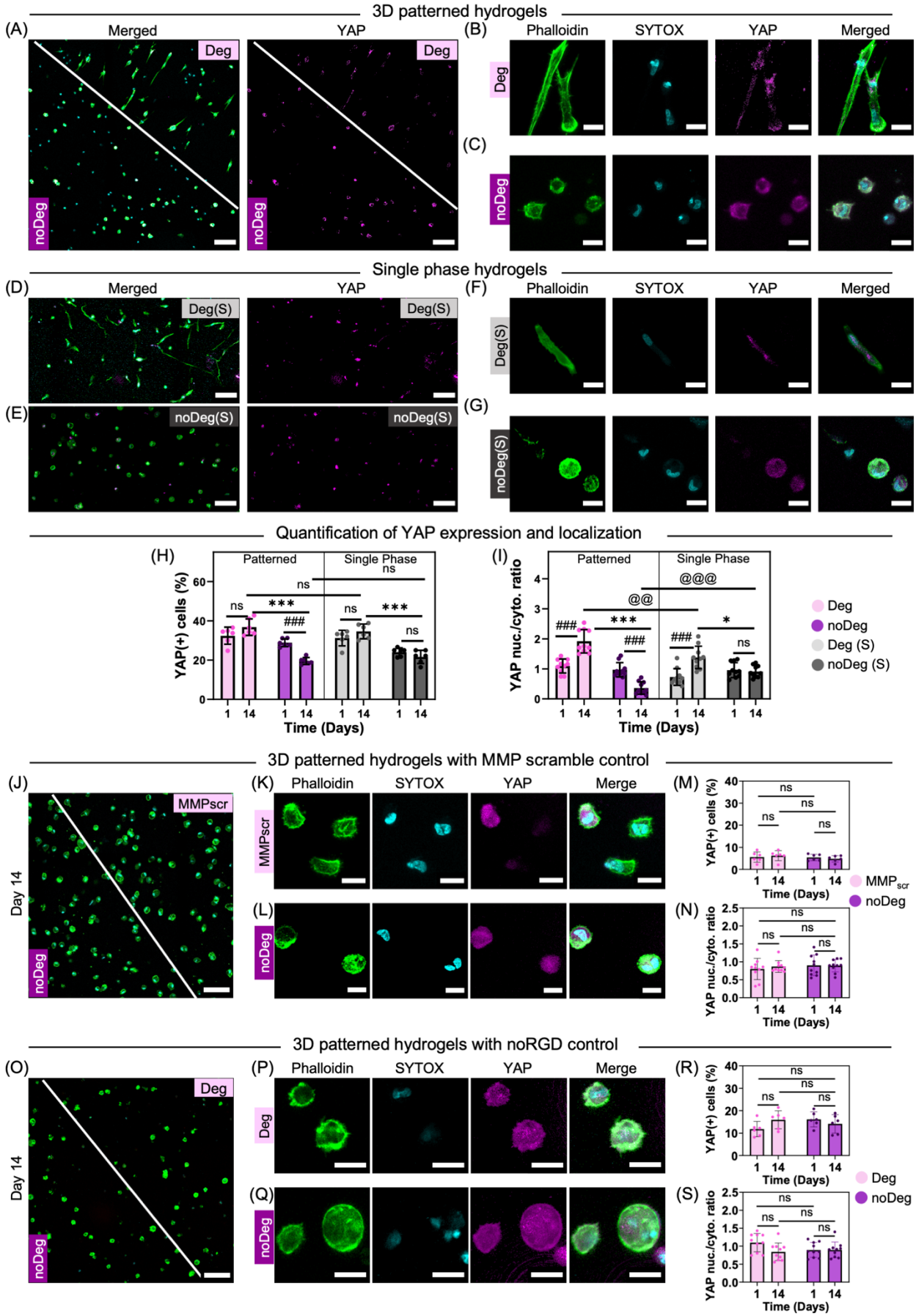
3D patterned hydrogels
(A)
Merged
YAP
Deg
noDeg
(B)
Phalloidin
SYTOX
YAP
Merged
Deg
(C)
noDeg
Single phase hydrogels
(D)
Merged
YAP
Deg(S)
(E)
noDeg(S)
(F)
Phalloidin
SYTOX
YAP
Merged
Deg(S)
(G)
noDeg(S)
Quantification of YAP expression and localization
(H)
Patterned
Single Phase
YAP(+) cells (%)
Time (Days)
(I)
YAP nuc./cyto. ratio
Time (Days)
Deg
noDeg
Deg (S)
noDeg (S)
3D patterned hydrogels with MMP scramble control
(J)
MMPscr
Day 14
noDeg
(K)
Phalloidin
SYTOX
YAP
Merge
MMPscr
(L)
noDeg
(M)
YAP(+) cells (%)
Time (Days)
MMPscr
noDeg
(N)
YAP nuc./cyto. ratio
Time (Days)
3D patterned hydrogels with noRGD control
(O)
Deg
Day 14
noDeg
(P)
Phalloidin
SYTOX
YAP
Merge
Deg
(Q)
noDeg
(R)
YAP(+) cells (%)
Time (Days)
Deg
noDeg
(S)
YAP nuc./cyto. ratio
Time (Days)

855

856 **Figure 7: YAP expression and nuclear to cytoplasmic localization of encapsulated hMSCs in**
857 **patterned materials vs. single-phase materials, and controls with MMP scramble peptide and**
858 **without RGD on day 14.** hMSC staining with actin (Phalloidin/green), nucleus (SYTOX/cyan) and
859 YAP expression (magenta). YAP expression in patterned materials: overview (A), representative
860 single cell images in the Deg (B) and noDeg (C) phase. YAP expression in single-phase materials:
861 overview of Deg (D) and noDeg (E) and representative single cells in Deg (F) and noDeg (G)
862 materials. Comparison between patterned and single-phase materials of YAP expression (H) and
863 nuclear to cytoplasmic localization (I). YAP expression in patterned materials with MMPscr control:
864 overview (J) and representative single cell images in Deg (K) and noDeg (L) regions. Quantification
865 of YAP expression (M) and YAP localization (N) in MMPscr materials. YAP expression in patterned
866 materials with noRGD control: overview (O) and representative single cell images in Deg (P) and
867 noDeg (Q) regions. Quantification of YAP expression (R) and YAP localization (S) in noRGD
868 materials. Bar plots show the mean and standard deviation of $n = 6$ fields of view containing $n > 120$
869 cells (H, M, R) and of $n = 10$ representative single cells from Deg vs. noDeg regions (I, N, S).
870 Statistical significance with ANOVA and Bonferroni correction. Scale bar: 100 µm (A, D, E, J, O)
871 and 20 µm (B, C, F, G, K, L, P, Q).

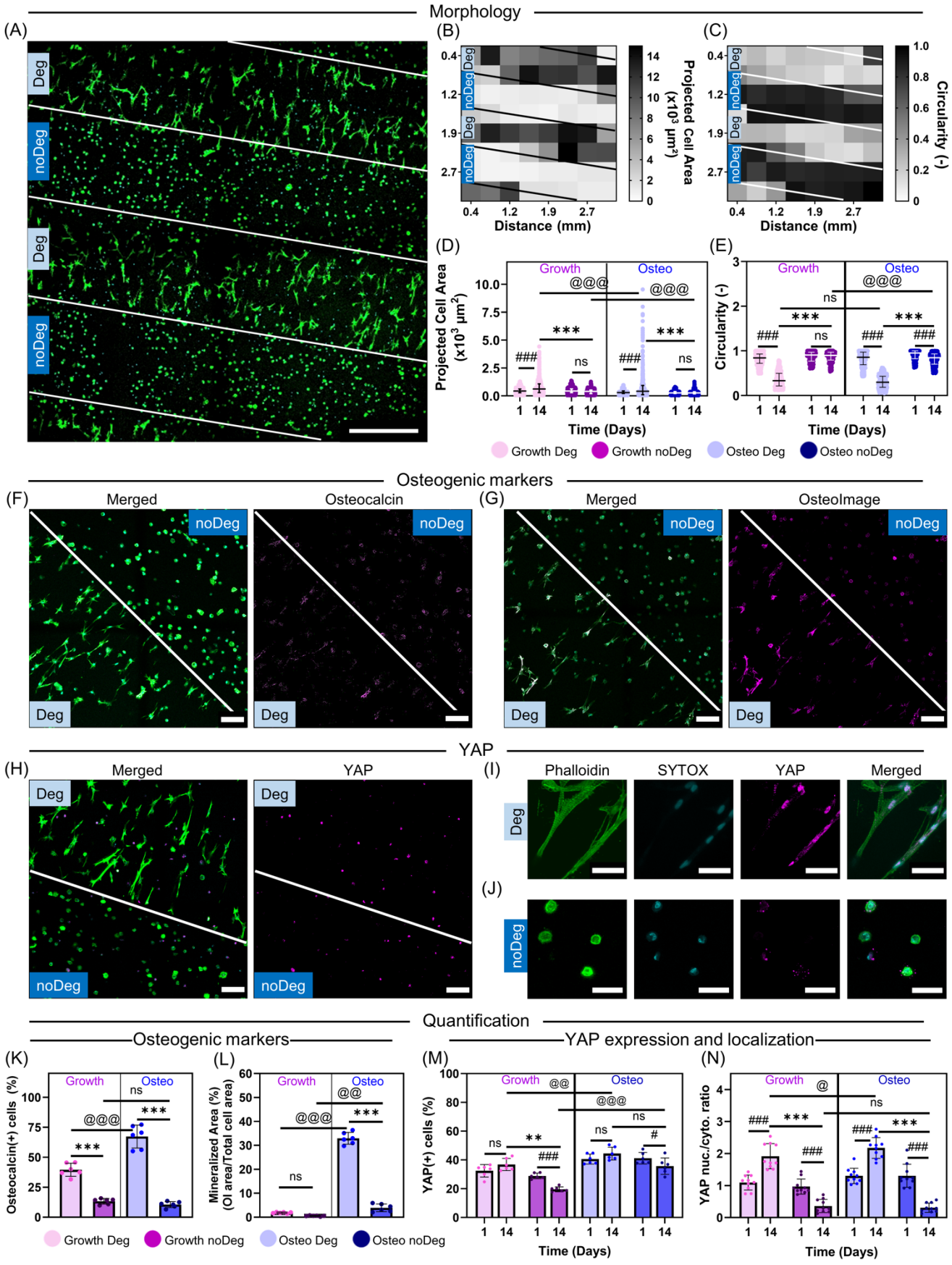
Morphology
(A)
Deg
noDeg
Deg
noDeg
(B)
Projected Cell Area (x10³ µm²)
Distance (mm)
(C)
Circularity (-)
Distance (mm)
(D)
Projected Cell Area (x10³ µm²)
Growth
Osteo
Time (Days)
(E)
Circularity (-)
Growth
Osteo
Time (Days)
Growth Deg
Growth noDeg
Osteo Deg
Osteo noDeg
Osteogenic markers
(F)
Merged
Osteocalcin
(G)
Merged
OsteoImage
YAP
(H)
Merged
YAP
(I)
Phalloidin
SYTOX
YAP
Merged
(J)
Quantification
Osteogenic markers
YAP expression and localization
(K)
Osteocalcin(+) cells (%)
(L)
Mineralized Area (%) (Ol area/Total cell area)
(M)
YAP(+) cells (%)
Time (Days)
(N)
YAP nuc./cyto. ratio
Time (Days)
Growth Deg
Growth noDeg
Osteo Deg
Osteo noDeg

872

873 **Figure 8: Enhanced cell response in patterned materials by osteogenic media on day 14.**
874 Representative actin (Phalloidin/green) and nucleus (SYTOX/cyan) staining of patterned materials
875 with hMSCs in osteogenic media (A). Heatmap quantification with an 8x8 grid of projected cell area
876 (B) and cell circularity (C). Dot graph of growth vs osteogenic media of cells in patterned materials
877 (> 400 single cells per phase and condition) of projected cell area (D) and circularity (E) on day 14
878 (see Suppl. Fig. S4D-F for corresponding images and heat maps on day 1). Representative
879 Osteocalcin (magenta, F) or Osterix (magenta, G) staining and expression quantification of OCN (K)
880 and mineralization (L). Representative YAP staining overview (H) and single cells from Deg (I) and
881 noDeg (J) sections. Quantification fraction of YAP(+) cells (M) and YAP localization (N). Dot
882 graphs show statistical significance with Kruskal-Wallis and Dunn's correction and bar plots
883 evaluated with statistical significance with ANOVA and Bonferroni correction. Scale bar: 500 µm
884 (A), 250 µm (F, G, H) and 20 µm (I, J).

885